JℳM PAPERS

Energy-based characterisation of large-scale coherent structures in turbulent pipe flows

D. Massaro[1,†], **J. Yao**[2,3], **S. Rezaeiravesh**[4], **F. Hussain**[3] **and P. Schlatter**[1,5]

[1]SimEx/FLOW, Engineering Mechanics, KTH Royal Institute of Technology, Stockholm 100 44, Sweden

[2]Advanced Research Institute of Multidisciplinary Sciences, Beijing Institute of Technology, Beijing 100081, China

[3]Department of Mechanical Engineering, Texas Tech University, Lubbock, TX 79409, USA

[4]Department of Fluids and Environment/MACE, The University of Manchester, Manchester M13 9PL, UK

[5]Institute of Fluid Mechanics (LSTM), Friedrich–Alexander–Universität (FAU) Erlangen–Nürnberg, Erlangen 91058, Germany

Large-scale coherent structures in incompressible turbulent pipe flow are studied for a wide range of Reynolds numbers ($Re_\tau = 180, 550, 1000, 2000$ and 5200). Employing the Karhunen–Loève decomposition and a novel approach based on the Voronoi diagram, we identify and classify statistically coherent structures based on their location, dimensions and Re_τ. With increasing Re_τ, two distinct classes of structures become more energetic, namely wall-attached and detached eddies. The Voronoi methodology is shown to delineate these two classes without the need for specific criteria or thresholds. At the highest Re_τ, the attached eddies scale linearly with the wall-normal distance with a slope of approximately $l_y \sim 1.2y/R$, while the detached eddies remain constant at the size of $l_y \approx 0.26R$, with a progressive shift towards the pipe centre. We extract these two classes of structures and describe their spatial characteristics, including radial size, helix angle and azimuthal self-similarity. The spatial distribution could help explain the differences in mean velocity between pipe and channel flows, as well as in modelling large and very-large-scale motions (LSM and VLSM). In addition, a comprehensive description is provided for both wall-attached and detached structures in terms of LSM and VLSM.

Key words: pipe flow, turbulence simulation, turbulence theory

† Email address for correspondence: dmassaro@kth.se

1. Introduction

Turbulent flows, although chaotic, are dominated by organised, vortical motions popularly known as coherent structures (Brown & Roshko 1974). In a turbulent flow field, a coherent structure can be defined as the spatial domain over which, underlying the randomly fluctuating vorticity field, there is instantaneous coherent vorticity (Hussain 1986). Instantaneous snapshots of coherent structures were educed by Hussain (1986) from the three-dimensional vorticity fields in a variety of shear flows in the laboratory and in silico. The near-wall turbulence has been extensively studied in the past, concluding that there is competition among different mechanisms (Kim, Kline & Reynolds 1971; Hamilton, Kim & Waleffe 1995; Schoppa & Hussain 2002). In particular, the autonomous streak cycle dominates, consisting of coherent low-speed streaks that regenerate quasi-streamwise vortices (Jeong *et al.* 1997; Jiménez & Pinelli 1999). However, in the logarithmic and outer layers, our knowledge of the various coherent structures is still limited. Based on two-dimensional visualisations, Kovasznay, Kibens & Blackwelder (1970), Adrian, Meinhart & Tomkins (2000) and Deng *et al.* (2018) observed indications of coherent hairpin packets, i.e. clusters of attached loop-like vortical structures, partially self-amplifying. To what extent the hairpin vortices are statistically relevant structures in fully turbulent flows is still a matter of debate (Schlatter *et al.* 2014; Eitel-Amor *et al.* 2015). Subsequent works (Del Álamo & Jiménez 2003; Balakumar & Adrian 2007; Monty *et al.* 2007) reported and described large-scale motions (LSMs) and very-large-scale motions (VLSMs). Large-scale motions are eddies resulting from the alignment of boundary layer vortices that travel at a common convective velocity with a region of low-momentum fluid among themselves (with a streamwise wavelength $< 3R$), while VLSM are long meandering regions of low- and high-speed momentum in channels and pipes (with a streamwise extent $> 3R$). Note that R is the pipe radius and an equivalent definition is found for channel and boundary layer flows based on the channel half-height and the boundary layer thickness, respectively. Hutchins & Marusic (2007) defined the superstructures in a turbulent boundary layer (TBL), equivalent to VLSM and with an extension larger than 10 times of the boundary layer thickness. Differences in the VLSM were observed between internal and external flows. As expected, structures in internal geometries exhibit less meandering compared with the TBL's motions, leading to larger length scales (Deshpande *et al.* 2021).

In an attempt to model the statistical behaviour of the coherent motions, Townsend (1951, 1961, 1976) first introduced the attached eddy hypothesis (AEH), i.e. geometrically self-similar attached eddies, which exist over a range of scales limited by the TBL thickness, i.e. by the Reynolds number. The AEH deserves careful consideration as it applies only to asymptotically high-Reynolds-number wall-bounded flows, where the inertial scales (large compared with the viscous length) populate the log region. However, no property about the shape and the organisation of the eddies is provided directly by the AEH. Despite the attached eddies model being effective in estimating flow statistics within the logarithmic range, accurately classifying the attached eddies by this model is challenging. The approach employed to extract these eddies, which may involve reliance on self-similarity or wall-attachment criteria, has the potential to reveal a variety of structures. Del Álamo *et al.* (2006) classified geometrically self-similar vortex clusters, i.e. groups of neighbouring points where the discriminant of the velocity gradient tensor exceeds a certain fraction of its root-mean-square value in the wall-parallel plane. Lozano-Duràn, Flores & Jiménez (2012) generalized the quadrant analysis to three dimensions by considering the intense Q events that contribute most to the tangential Reynolds stress in plane turbulent channels. The quadrant analysis, as originally introduced by Wallace,

Eckelman & Brodkey (1972) and Willmarth & Lu (1972), is typically employed to categorise data points based on their location within the parameter plane defined by streamwise and wall-normal velocity fluctuations, represented as u and v in the context of plane channel flow. The identification of Q1 events (outward interactions, ($u > 0$, $v > 0$)), Q2 events (ejections, ($u < 0$, $v > 0$)), Q3 events (inward interactions, ($u < 0$, $v < 0$)) and Q4 events (sweeps, ($u > 0$, $v < 0$)) relies on a user-defined threshold. More recently, using a data-driven approach, Cheng *et al.* (2019) identified modes that resemble Townsend's attached eddies. They employed the adaptive mode decomposition, known as bidimensional empirical mode decomposition, which in principle does not necessitate a predefined set of basis functions, but still needs a threshold value.

Other studies aimed at going beyond the AEH, attempting to model eddies that are not wall attached (Robinson 1991). Indeed, wall-attached eddies represent only a facet of the puzzle and do not offer a complete description of wall-bounded flows. Perry & Marusic (1995) enhanced the attached eddy model through the integration of three distinct categories of eddies. Particularly, in addition to the type A, labelled as 'wall structures' (wall-attached eddies) whose vortex lines extend to the wall, they introduced the type B, referred to as 'wake structures' (wall-detached eddies) that do not reach the boundary, and the type C, also called Kolmogorov-scale eddies, which contribute to the high-wavenumber motions. Expanding upon Perry & Marusic (1995), Baars & Marusic (2020*a*,*b*) introduced a data-based spectral decomposition method that employs two spectral filters to distinguish type-A and type-B eddies. In a recent study, Hu, Yang & Zheng (2020) explored the statistical properties of detached eddies, proposing a model that represents these eddies as flow structures centred at the midpoint of the log layer.

In the context of data-driven techniques, proper orthogonal decomposition (POD) has been demonstrated to be effective in the detection of both attached and detached eddies (Wang, Pan & Wang 2022*a*; Wang *et al.* 2022*b*). For turbulent pipe flows, Hellström, Sinha & Smits (2011) employed particle image velocimetry (PIV), focusing on radial–azimuthal planes and employing Taylor's hypothesis. Their findings indicated that by reconstructing the flow field using the 10 most energetic POD modes, they could effectively capture all the fundamental characteristics of a VLSM. This suggests that VLSMs are primarily composed of the most energetic POD modes, giving rise to the appearance of extensive meandering structures. Additionally, the four most energetic modes bear a resemblance to a combination of two helical response modes identified through the linear stability analysis by McKeon & Sharma (2010) and Sharma & McKeon (2013). Hence, Hellström *et al.* (2011) endorsed the linear mechanisms associated with the propagating response modes proposed by McKeon & Sharma (2010). Similarly, Große & Westerweel (2011) employed PIV measurements to study structures within pipe flows, providing compelling evidence of highly extended streamwise velocity structures. Their findings further confirmed the existence of low- and high-speed regions extending across several pipe radii in the streamwise direction. More recently, Hellström, Marusic & Smits (2016) presented evidence of a geometric self-similarity in certain POD modes and identified a universal length scale that characterises these modes. This length scale is found to scale with the distance from the wall. All of the aforementioned experimental studies face similar limitations. Firstly, they rely on Taylor's hypothesis to deduce streamwise spatial variations from two-dimensional fields collected at short time intervals. Consequently, significant discrepancies can arise when comparing instantaneous fields with those generated using Taylor's hypothesis (Zaman & Hussain 1981; Wu, Baltzer & Adrian 2012). Secondly, the measurement of the velocity near the wall poses challenges. Given these experimental constraints, data from direct numerical simulations (DNS) are particularly well suited for examining the characteristics of LSMs and VLSMs. Earlier, Duggleby *et al.* (2007),

Duggleby, Ball & Schwaenen (2009), Bailey & Smits (2010) and Baltzer, Adrian & Wu (2013) conducted DNS to investigate structures in turbulent pipe flows at moderate Reynolds numbers, proposing a classification between propagating and non-propagating POD modes. However, the moderate Reynolds number and the reduced domain sizes were the main limitations of previous DNS.

In this study we examine a comparably long pipe ($L_z = 10\pi R$) across a wide range of five Reynolds numbers, spanning from $Re_\tau = 180$ to 5200, the highest ever considered for such dimensions. The friction Reynolds number is based on the friction velocity (u_τ), the pipe radius (R) and the kinematic viscosity (ν). In particular, we show that the POD effectively distinguishes between wall-attached and detached eddies based on their energy content. Introducing a novel methodology based on Voronoi analysis, we eliminate the need for velocity filtering (Perry & Marusic 1995; Lee & Moser 2019; Baars & Marusic 2020*a,b*) or defining intense events using a specific threshold (Moisy & Jiménez 2004; Lozano-Duràn *et al.* 2012; Atzori *et al.* 2018). This is especially relevant when the Reynolds number is moderately high. From the two-point spatial (temporal) correlation tensor of statistically converged data, the POD extracts statistical eddies (space eigenfunctions) along with their corresponding (linearised) dynamics (time coefficients). The extracted spatial functions, known as POD modes, are coherent structures representing 'the deterministic function which is best correlated on average with the velocity realisations' (Lumley 1967). Following Jiménez (2018), these should be termed 'compact eddies', denoting an expansion based on an energy-optimal basis where no dynamics is included. However, it is crucial to realise that the dynamics of the linear modal representation can be assimilated by extracting the corresponding temporal coefficients. Throughout the rest of this paper, we use the terms eddy and structure interchangeably. This is because, in their statistical and linearised representation, the POD modes encompass both aspects (Massaro 2024).

The remainder of the paper is organised as follows. First, numerical simulations are detailed in § 2, followed by a brief review of the Karhunen–Loève (KL) decomposition in § 3. Section 4 discusses the main findings of turbulent pipe flows at various Reynolds numbers ($Re_\tau = 180, 550, 1000, 2000, 5200$). The novel methodology for quantifying the density of POD modes in the radial direction, as introduced by Massaro *et al.* (2024), is discussed, and the characteristics of the attached and detached eddies are explored. Concluding remarks are in § 5.

2. Direct numerical simulations

The large-scale coherent structures in turbulent pipe flow at various Reynolds numbers are studied by using the DNS datasets of incompressible turbulent pipe flows. The simulations were conducted with the pseudo-spectral code `Openpipeflow` (Willis 2017). The primitive-variable solver uses a cylindrical coordinate system, where the radial, axial and azimuthal directions are denoted by r, z and θ, respectively; $y = R - r$ is the wall-normal distance. The momentum equations for the corresponding u_r, u_z and u_θ velocity components are time-integrated coupled with the pressure-Poisson equation and supplemented by proper initial and boundary conditions. Periodic boundary conditions are set in the axial (streamwise) direction and, at the wall, the no-slip and impermeability conditions are imposed. A second-order semi-implicit time-stepping scheme is adopted for time marching.

In the space representation, a Fourier discretisation is used in z and θ, whereas a high-order central finite-difference scheme with a nine-point stencil is used in the radial direction. The number of grid points in the radial direction (N_r) and the number of Fourier

Re_τ	Re_b	$N_r \times N_\theta \times N_z$	$\Delta t U_b/R$	N	$\Delta T U_b/R$	$\tilde{k}$	k	$k_\%$
180	5300	$192 \times 256 \times 1024$	0.01	178	2	0.0147	0.0168	87.5 %
550	19 000	$256 \times 768 \times 2048$	0.005	101	2	0.0074	0.0126	58.7 %
1000	37 700	$384 \times 1280 \times 3072$	0.002	82	4	0.0048	0.0112	42.9 %
2000	83 000	$768 \times 2560 \times 6144$	0.001	88	2	0.0028	0.0101	27.8 %
5200	240 000	$1024 \times 5120 \times 12\,288$	0.0005	77	2	0.0023	0.0085	27.1 %

Table 1. Numerical details of the DNS data sets: the friction Reynolds number Re_τ, the bulk Reynolds number Re_b ($Re_b = 2U_b R/\nu$), the spatial resolutions ($N_r \times N_\theta \times N_z$) and the time step for the time integration ($\Delta t U_b/R$). Numerical details of the modal decomposition: the number of collected snapshots (N), the time interval between snapshots ($\Delta T U_b/R$), the kinetic energy contained in the first $\{N_\theta \times N_z\} = \{32, 32\}$ modes ($\tilde{k}$), the total kinetic energy estimated from the statistics (Yao *et al.* 2023) and the percentage of total kinetic energy captured from the first 32^2 POD modes ($k_\% = \tilde{k}/k$).

modes in the axial (N_z) and azimuthal (N_θ) directions have been carefully assessed to ensure a DNS resolution and to capture the smallest spatial scales (Yao *et al.* 2023); see also table 1. In physical space the number of grid points in the axial and azimuthal directions is increased by a factor of $3/2$ to account for dealiasing. The grid points are distributed radially with a hyperbolic tangent function, ensuring precise resolution of steep wall-normal velocity gradients within the viscous layer. Furthermore, points near $r = 0$ are clustered to preserve the high-order characteristics of the finite-difference scheme near the pipe's axis. The computational domain is significantly longer than in the previous DNS available in the literature to capture the largest motions; a topic we revisit later in the paper. The axial extension is $L_z = 10\pi R$, based on the pipe radius. The flow is driven by a variable pressure gradient, adjusted to ensure a constant mass flux through the pipe. Further details on the implementation are given by Willis (2017).

A set of five different simulations are used in the present study, performed at $Re_\tau \approx 180$, 550, 1000, 2000 and 5200, where $Re_\tau = u_\tau R/\nu$ is the friction Reynolds number. The one-point statistics and one-dimensional energy spectra are reported by Yao *et al.* (2023), where a comprehensive comparison with the numerical and experimental state of the art is provided. Yao *et al.* (2023) also reported the time-averaging uncertainty that is estimated using the method by Oliver *et al.* (2014) and Rezaeiravesh *et al.* (2022).

3. Karhunen–Loève decomposition

Originally developed by Karhunen (1947) and Loève (1948) in the 1940s, the KL modal decomposition is a bi-orthogonal stochastic process expansion. Commonly referred to as both principal component analysis and POD, the KL decomposition seeks to approximate a generic vector function $\boldsymbol{u}(\boldsymbol{x}, t)$, with $\boldsymbol{x} = (r, \theta, z)$, over a domain of interest $\mathcal{D} = \Omega \times [0, T]$ as a finite sum of functions of variables separated in space $\boldsymbol{x}$ and time t. The finite spatial domain is indicated by Ω. This is achieved through the minimisation of residual energy between the nonlinear field, which comprises the collected snapshots, and its linear representation (Tropea, Yarin & Foss 2007). The KL expansion generates (POD) modes that are designed to be the orthogonal basis representing the optimal energy projection of the most dominant flow features. The spatial orthogonality condition and the hierarchical description of fluctuating energy within statistical structures are fundamental aspects of this modal decomposition. We adopt the snapshot POD method outlined by Sirovich (1987*b*), which enables the analysis of three-dimensional flows with a number of grid points significantly larger than the number of snapshots, unlike the classical POD

method introduced by Lumley (1970). In contrast to the three-dimensional snapshot POD, the KL decomposition first exploits the two space homogeneities in the pipe flow, i.e. in the azimuthal and axial directions.

The derivation follows the work by Webber, Handler & Sirovich (1997) for the minimal channel flow. First, we Fourier expand the velocity field $\boldsymbol{u}(\boldsymbol{x}, t)$ in z and θ,

$$
\begin{aligned}
\boldsymbol{u}(r, \theta, z, t) &= \sum_{\kappa_\theta=-\infty}^{\infty} \sum_{\kappa_z=-\infty}^{\infty} \hat{\boldsymbol{u}}_{(\kappa_\theta, \kappa_z)}(r, t) \exp(2\pi i \kappa_\theta \theta / L_\theta) \exp(2\pi i \kappa_z z / L_z) \\
&= \sum_{p=1}^{\infty} \hat{\boldsymbol{u}}_p(r, t) \exp(2\pi i \kappa_\theta \theta / L_\theta) \exp(2\pi i \kappa_z z / L_z),
\end{aligned}
\tag{3.1}
$$

where $(\kappa_\theta, \kappa_z)$ indicates a wavenumber pair with the azimuthal and streamwise (axial) wavenumbers, and L_θ and L_z are the domain lengths in the corresponding directions. The Fourier transforms of $\boldsymbol{u}$ in the axial and azimuthal directions $\hat{\boldsymbol{u}}_{(\kappa_\theta, \kappa_z)}$ are functions of the radial distance and time for a given pair of $(\kappa_\theta, \kappa_z)$. The expansion is recast as a function of the index p, which corresponds to the wavenumber pair $(\kappa_\theta, \kappa_z)$. The index p spans only the positive quadrant ($\kappa_\theta \geq 0, \kappa_z \geq 0$) since all modal solutions can be derived from the eigenmodes found within a single quadrant of the wavenumber space, exploiting the statistical invariance of the pipe flow under axial shift and azimuthal rotation (Sirovich 1987a). The index p varies between 1 and $\hat{N}$, i.e. the number of pairs in the positive wavenumbers space. In the inhomogeneous radial direction, each term $\hat{\boldsymbol{u}}_p(r, t)$ in (3.1) is modally decomposed into spatial and temporal components:

$$
\hat{\boldsymbol{u}}_p(r, t) = \sum_{q=1}^{\infty} \hat{a}_{(q,p)}(t) \hat{\boldsymbol{\Phi}}_{(q,p)}(r).
\tag{3.2}
$$

Here $\hat{a}_{(q,p)}(t)$ and $\hat{\boldsymbol{\Phi}}_{(q,p)}(r)$ are the time coefficients and the space functions, respectively. The space functions form a set of orthonormal bases obtained from the eigenfunctions that minimise, in the least squares sense, the residual energy between the nonlinear field and its linear representation. The index q, called quantum index (Webber *et al.* 1997), ensures to include all realisations and symmetries ($\tilde{N}$), where $\tilde{N}$ is $2N$ and not $4N$ because the azimuthal homogeneity is imposed by considering only the positive quadrant. For a wavenumber pair p, the order of the modes goes from the most ($q = 1$) to the least ($q = \tilde{N}$) energetic one. Therefore, a specific eigenfunction associated with a wavenumber index pair is fully defined by the triplet $\boldsymbol{k} = (q, \kappa_\theta, \kappa_z) = (q, p)$.

The calculation of time coefficients $\hat{a}$ and spatial functions $\hat{\boldsymbol{\Phi}}$ involves transitioning from the current continuous to a discrete formulation. In the discrete framework the solution is represented using a finite number of grid points for a limited number of snapshots. Since the POD focuses on large scales, the original DNS resolution (Yao *et al.* 2023) is unnecessary. Additionally, it is impractical due to memory constraints. To address this, we perform data dimensionality reduction in the radial direction by downsampling the grid points, particularly for cases with the highest Reynolds numbers. The effect of the downsampling and the temporal convergence of the POD modes have been carefully assessed (Massaro *et al.* 2024). Similarly to Hellström *et al.* (2016), a reduced set of axial and azimuthal wavenumbers is kept, in particular, the first 32 modes in each direction. The corresponding percentage of the total kinetic energy ($\tilde{k}$) contained in $\{N_\theta = 32, N_z = 32\}$ is calculated; see table 1. After conducting Fourier transforms in the axial and azimuthal

directions for each snapshot, the snapshot matrix is assembled. The snapshot matrix $\hat{U}_p$ is constructed only for $p = (\kappa_\theta \geq 0, \kappa_z \geq 0)$ by stacking the Fourier coefficients of each snapshot into a single column vector. For any given pair p, the snapshot matrix appears as

$$\hat{U}_p = [\hat{u}_0, \hat{u}_1, \ldots, \hat{u}_{m-1}] \in \mathbb{C}^{n \times m}, \tag{3.3}$$

where $n = n_r \times n_{vel}$ is the number of radial points (n_r) times the number of velocity components ($n_{vel} = 3$) and $m = 2N$ is the double number of snapshots. The snapshots were sampled at constant intervals of $\Delta T U_b / R = 2$ (for almost all Reynolds numbers; see table 1) over a duration that encompasses the slowest frequency according to the Nyquist criterion. It is analytically established that the spatial eigenfunctions are derived from the singular value decomposition (SVD) of the matrix (3.3). Note that each column of $\hat{X}_p \in \mathbb{C}^{n \times m}$ and $\hat{T}_p \in \mathbb{C}^{m \times m}$ corresponds to a specific $\hat{\Phi}_{(q,p)}(r)$ and $\hat{a}_{(q,p)}(t)$ in the continuous formulation. The orthogonal basis function $\hat{X}_p$ and the corresponding time coefficients $\hat{T}_p$ are computed via SVD of the snapshot matrix as

$$\hat{U}_p = \hat{X}_p \Sigma_p \hat{W}_p^*, \tag{3.4}$$

where the matrix $\hat{W}_p^* \in \mathbb{C}^{m \times m}$ is the right singular vectors matrix (* indicates the conjugate transpose) and $\Sigma_p \in \mathbb{R}^{m \times m}$ is the diagonal matrix of singular values of $\hat{U}_p$ (i.e. the energies). The time coefficients are retrieved as

$$\hat{T}_p = \Sigma_p \hat{W}_p^*. \tag{3.5}$$

To ensure that each mode has unit energy, proper normalisation must be considered:

$$\|\hat{X}_p\|_M = I, \quad \|\hat{W}_p\|_N = I. \tag{3.6a,b}$$

Here $M \in \mathbb{R}^{n \times n}$ and $N \in \mathbb{R}^{m \times m}$ are the mass and the temporal weight matrix, respectively, and I is the identity matrix. When the snapshots are collected with equidistant time intervals, N is the identity matrix $N = I$. The mass matrix M contains the volume quadrature weights $dV = r \, dr \, d\theta$. The unit energy normalisation is obtained by considering $M^{1/2} \hat{U}_p N^{1/2}$ into (3.4) and decomposing as

$$M^{1/2} \hat{U}_p N^{1/2} = \widehat{X}_p \Sigma_p \widehat{W}_p^*, \tag{3.7}$$

where $\widehat{X}_p^* \widehat{X}_p = I$ and $\widehat{W}_p^* \widehat{W}_p = I$. Note that $\widehat{X}_p$ and $\widehat{W}_p^*$ are different from $\hat{X}_p$ and $\hat{W}_p^*$ as the mass and temporal weight matrices are considered. Eventually, the modes are reconstructed as

$$\hat{X}_p = M^{-1/2} \widehat{X}_p, \tag{3.8}$$

with unit energy and orthogonal to each other, while the time coefficients are

$$\hat{T}_p = \Sigma_p (N^{-1/2} \widehat{W}_p)^* = \Sigma_p \hat{W}_p^*, \tag{3.9}$$

where the energies are given by the diagonal matrix Σ_p. For each wavenumber pair p, the matrix Σ_p contains $\tilde{N}$ energies $\lambda_{(q,p)}$ that are ordered according to the quantum index q; where $q = 1$ is the most energetic POD mode for a pair $p = (\kappa_\theta, \kappa_z)$.

Moreover, for determining the overall energy ranking, it is essential to consider the proper degeneracy, denoted as d^k. This is particularly crucial as we perform the SVD for only the first quadrant of the wavenumber space. It has been established that
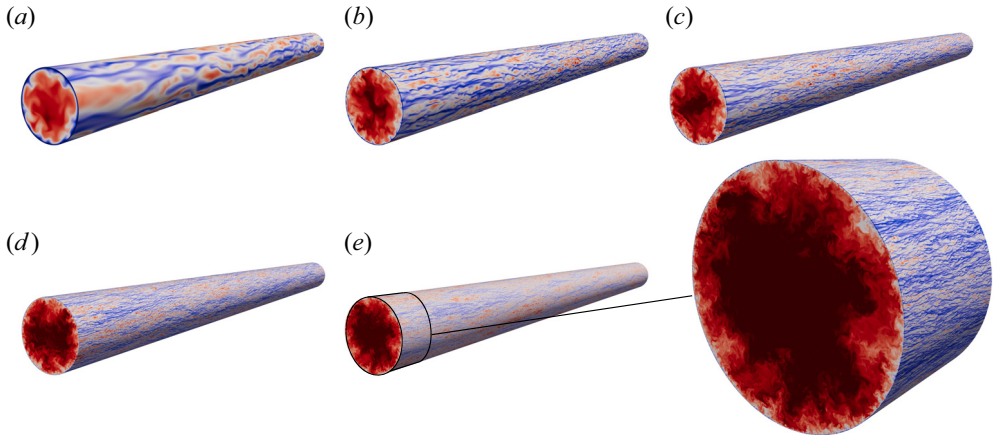
Figure 1. Instantaneous streamwise velocity contours (u_z) with low- and high-speed velocity streaks in blue and red, respectively. Panels (*a–e*) show a cross-stream plane and a near-wall cylindrical shell ($y^+ \approx 15$) at $Re_\tau = 180, 550, 1000, 2000$ and 5200.

an eigenvalue $\lambda_{(q,(\kappa_\theta,\kappa_z))}$ is equal to the eigenvalues in the other quadrants, namely $\lambda_{(q,(\kappa_\theta,-\kappa_z))}$, $\lambda_{(q,(-\kappa_\theta,\kappa_z))}$ and $\lambda_{(q,(-\kappa_\theta,-\kappa_z))}$; see Webber *et al.* (1997). Therefore, the contribution to the total kinetic energy of a specific triple, denoted as $\boldsymbol{k} = (q, p)$, is determined by $e^{\boldsymbol{k}} = d^{\boldsymbol{k}}\lambda(q, p)$. In particular, the degeneracy is defined as $d^{\boldsymbol{k}} = 1, 2$ and 4 for $(\kappa_\theta = 0, \kappa_z = 0)$, $(\kappa_\theta \neq 0, \kappa_z = 0)$ and $(\kappa_\theta = 0, \kappa_z \neq 0)$, and $(\kappa_\theta \neq 0, \kappa_z \neq 0)$. The importance of degeneracy is further emphasised in the reconstruction of the flow field, as discussed by Massaro *et al.* (2024). Note that, hereafter, the percentage of energy contribution, $f(\%)$, can be calculated by normalising $\lambda_{(q,p)}$ with respect to the total kinetic energy (k) obtained from DNS statistics.

4. Results

We begin with an overview of the instantaneous flow evolution as the Reynolds number increases. A characterisation of large-scale statistically coherent structures is then provided by using an energy-based classification of the structures. We analyse the radial shapes of the POD modes obtained through the KL decomposition and order these modes based on their contributions to the total kinetic energy. In particular, we focus on the four Reynolds numbers $Re_\tau = 180, 550, 2000$ and 5200 since the intermediate $Re_\tau = 1000$ does not provide further insights. At the lowest Reynolds numbers the results have been assessed by Massaro *et al.* (2024), showing an excellent agreement with the literature (Duggleby *et al.* 2007, 2009), and also discussing the limitations of previous classifications. Presented here is a novel Voronoi-based analysis that enables the extraction of two classes of modes: wall-attached (or simply attached) and detached eddies. Finally, the key properties of these structures are discussed.

4.1. *Instantaneous flow visualisation*

Observing the instantaneous flow reveals the emergence of numerous spatial scales as Re_τ increases. Figure 1 shows streamwise velocity u_z contours in a cross-stream plane and on a near-wall cylindrical shell at $y^+ \approx 15$ ($y^+ = (R - r)^+$), similar to Pirozzoli *et al.* (2021) but with a much longer axial extent.

	$Re_\tau = 180$				$Re_\tau = 550$				$Re_\tau = 1000$				$Re_\tau = 2000$				$Re_\tau = 5200$			
	κ_θ	κ_z	q	$f(\%)$	κ_θ	κ_z	q	$f(\%)$	κ_θ	κ_z	q	$f(\%)$	κ_θ	κ_z	q	$f(\%)$	κ_θ	κ_z	q	$f(\%)$
1	6	1	1	1.087	3	1	1	0.712	2	1	1	0.809	3	0	1	0.745	3	0	1	0.881
2	4	1	1	1.009	2	1	1	0.600	1	1	1	0.572	2	2	1	0.498	2	1	1	0.668
3	2	1	1	0.983	4	2	1	0.524	2	4	1	0.438	4	2	1	0.479	5	1	1	0.612
4	5	1	1	0.969	2	2	1	0.479	1	3	1	0.437	4	1	1	0.424	3	2	1	0.539
5	3	1	1	0.785	3	0	1	0.453	1	2	1	0.418	4	3	1	0.388	1	0	1	0.523
6	4	2	1	0.730	4	1	1	0.442	3	0	1	0.340	1	1	1	0.373	1	1	1	0.429
7	5	2	1	0.653	1	1	1	0.399	1	0	1	0.336	3	2	1	0.286	4	2	1	0.357
8	3	2	1	0.619	3	2	1	0.362	2	3	1	0.332	2	1	1	0.277	3	1	1	0.350
9	8	2	1	0.591	3	3	1	0.339	2	2	1	0.308	5	2	1	0.271	4	4	1	0.239
10	7	1	1	0.571	2	3	1	0.300	1	4	1	0.246	5	1	1	0.218	4	1	1	0.236

Table 2. The 10 most energetic POD modes at $Re_\tau = 180, 550, 1000, 2000$ and 5200: the azimuthal and streamwise wavenumber (κ_θ, κ_z), the quantum index (q) and the fraction of the total fluctuating kinetic energy ($f = \lambda_{(q,p)}/k$, with $p = (\kappa_\theta, \kappa_z)$).

In the cross-stream planes the flow consistently exhibits a limited number of bulges distributed azimuthally. These low azimuthal wavenumber patterns correspond to regions where high-speed fluid enters from the pipe's core while low-speed fluid is ejected from the wall. As discussed below, their resemblance to the POD modes is quite striking, as previously reported at lower Reynolds numbers by Hellström, Ganapathisubramani & Smits (2015). In all cases, large scales dominate in the central region of the pipe. Figure 1 shows, among the multitude of small streaks, elongated regions of low and high velocity, in blue and red, respectively. These streaks have an average spacing of $(R\theta)^+ \approx 100$ and are elongated in z. In the near-wall cylindrical shell at $y^+ \approx 15$, streaks are observed with an arrangement visibly connected to the cross-stream pattern, as seen at $Re_\tau = 180$ in figure 1(*a*). As Re_τ increases, the scale separation gets larger, the near-wall streaks scale in wall units, and the centre modes scaling in integral scales become more and more distinct.

Decomposing the flow according to the KL expansion, we aim to understand the spatial (temporal) correlation between instantaneous structures. The near-wall dynamics of streaks have been extensively discussed in the past and the influence of the Reynolds number on the autonomous wall cycle is limited, if not entirely negligible (Jiménez & Pinelli 1999). Therefore, for the remainder of the paper, our focus is on the larger scales in the outer layer, rather than the buffer layer and viscous sublayer.

4.2. *The POD modes hierarchy*

The 10 most energetic modes at the five Reynolds numbers considered are listed in table 2. For each wavenumber pair (κ_θ, κ_z), the corresponding quantum index and the fraction of the fluctuating energy $f = \lambda_{(q,p)}/k$ are reported. The energy fraction is computed relative to the total fluctuating energy. Note that the mean flow is not subtracted in advance, thus, it corresponds to the zeroth POD mode, and it is not reported in table 2.

At the lowest Reynolds number ($Re_\tau = 180$), the most energetic modes are characterised by a large number of streaks in the cross-stream planes, with the azimuthal wavenumber varying from 2 to 8. The POD mode 1 corresponds to six pairs of streamwise streaks that qualitatively resemble the evenly distributed low-speed streaks in figure 2(*a*). Their maximum magnitude is located at $y^+ \approx 20$, with an azimuthal separation of $\Delta R\theta^+ \approx 85$

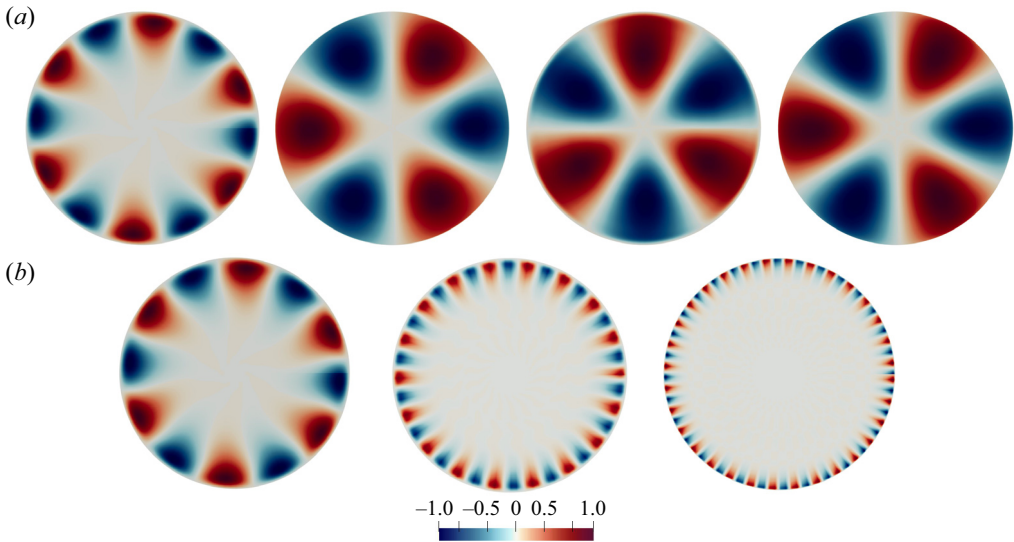(*a*)

(*b*)

−1.0 −0.5 0 0.5 1.0

Figure 2. (*a*) From left to right, cross-stream planes of the streamwise velocity of the most energetic POD modes $\hat{\Phi}_{(q=1,p)}(r)$ (normalised by their maximum) at $Re_\tau = 180, 550, 2000, 5200$. (*b*) Scaling of the most energetic POD mode at $Re_\tau = 180$, i.e. near-wall streaks, at higher Reynolds numbers $Re_\tau = 550$ and 1000.

and an axial wavelength of $\Delta z^+ \approx 1000$. The POD mode 1 makes a substantial contribution, approximately 1.1 %, to the total kinetic energy. Note that a single POD mode does not represent a dynamic flow feature, but it does provide an indication of the energetic level of such structures. Therefore, we have examined the evolution of the POD mode 1 as Re_τ increases to understand how the mode and its energetic contribution vary. Since only the first 32 modes in the axial and azimuthal directions are retained in the POD calculation, we can identify the equivalent mode at $Re_\tau = 550$ and 1000 only. At higher Reynolds numbers, the mode exhibits wavenumbers beyond 32. As one would expect, the mode shape is maintained, i.e. the mode resembles near-wall streaks, but the energy contribution drops significantly; see figure 2(*b*). This decrease occurs because larger structures in the outer layer contain the majority of the energy. The POD mode 342 ($\kappa_\theta = 18$, $\kappa_z = 3$) at $Re_\tau = 550$ and the POD mode 2382 ($\kappa_\theta = 32$, $\kappa_z = 6$) at $Re_\tau = 1000$, contribute only 0.0259 % and 0.0017 % to the total kinetic energy, respectively. The energy is spread across a wider range of scales with the larger scales containing a higher portion of the energy. As stated earlier, the energy contributions of multiple POD modes that describe a single dynamical feature, such as the streaks, should be combined.

When the Reynolds number increases, the energy contribution of the top-ranked modes, as the POD mode 1, gradually diminishes. Notably, starting from $Re_\tau = 550$, a mode with $\kappa_z = 0$ appears in table 2. This becomes the dominant mode at the highest Reynolds numbers, contributing 35 % more energy than the POD mode 2. Observe that an eddy with $\kappa_z = 0$ represents a structure with a wavelength longer than the entire pipe, despite the considerable length of the current set-up ($L_z = 10\pi R$). Modes with $\kappa_z = 0$ were previously classified by Duggleby *et al.* (2007) as non-propagating modes, and further categorised into shear ($\kappa_\theta = 0$) and roll ($\kappa_\theta \neq 0$) modes. The contribution of the non-propagating modes to the total fluctuating energy increases with the Reynolds number. In particular, these modes constitute approximately 1.6 % and 2.1 % of k at $Re_\tau = 2000$ and 5200, respectively. The shear modes contribute 0.38 % and 0.54 % at $Re_\tau = 2000$ and 5200,

996 A45-10

respectively, while the roll modes contribute more: 1.22 % and 1.56 % at $Re_\tau = 2000$ and 5200, respectively.

In general, a distinct pattern emerges: with increasing Reynolds numbers, structures that maintain spatial correlation over more than $3R$ become more energetically significant. These structures have been referred to as VLSMs in turbulent pipe flows (Adrian *et al.* 2000). Using an array of hot wires and operating under Taylor's hypothesis, Monty *et al.* (2007) also documented the existence of long meandering features in both pipe and channel flows. These features qualitatively resemble those observed in boundary layers, with lengths of the order of $O(20\delta)$ (Hutchins & Marusic 2007). Based on the above definition of the VLSM ($\lambda_z > 3R$), the VLSM contribution to the total k is seen to increase with Reynolds number, particularly reaching around 14 % and 16 % at $Re_\tau = 2000$ and 5200, respectively.

The VLSM with $\kappa_\theta = 3$ and $\kappa_z = 0$ appears as most energetic at $Re_\tau = 2000$ and 5200 and consistently ranks among the top six from $Re_\tau = 550$ to 5200. It is worth noting that this mode ($\kappa_\theta = 3$, $\kappa_z = 0$) has already been reported previously. Bailey & Smits (2010), despite not observing a clear distinction between VLSMs and LSMs, reported that a VLSM tends to be concentrated within the lower azimuthal modes, typically around $\kappa_\theta = 3$. This observation aligns with the large transverse scales reported in the spectrally filtered results, also discussed in Bailey & Smits (2010). In contrast, the LSM appears to be distributed across a broader range of azimuthal scales, hence, no dominant transverse scale and spanning a wide range of streamwise and transverse scales. Our results, covering a wider range of Reynolds numbers and higher values, support their observations, as illustrated by the mode hierarchy in table 2. This finding is also in line with other studies that consistently identify modes around ($\kappa_\theta = 3$, $\kappa_z = 0$) as the energetically dominant (Baltzer *et al.* 2013; Hellström *et al.* 2016). Furthermore, there may be a noteworthy connection with transitional pipe flow. Faisst & Eckhardt (2003) and Eckhardt *et al.* (2007) predicted that nonlinear travelling wave instabilities exhibiting threefold azimuthal symmetry are the first to appear with increasing Reynolds numbers, marking the transition to turbulence in pipe flow. Experimental observations by Hof *et al.* (2004) have also identified states with up to sixfold symmetry. Their findings align with the range of the azimuthal modes observed in the VLSM wavenumbers within turbulent flows. This suggests that the VLSMs stem from the persistence of unstable travelling waves that originate during the transition phase and continue into the turbulent flow regime. However, as discussed by Bailey & Smits (2010), some inconsistencies need to be considered. Firstly, the formation mechanism of these travelling waves in transitional flows is inherently unstable, making it challenging for these modes to persist in turbulent flows where the mean shear is significantly different. Secondly, the wavelengths observed by Faisst & Eckhardt (2003) are much shorter than those of the VLSM. This latter difference could be explained by the fact that the wavelength of the instability depends on the Reynolds number and azimuthal mode, generally increasing with higher Reynolds numbers and decreasing with higher azimuthal modes.

From our perspective, the persistence of the roll modes with $\kappa_\theta = 3$ at different Reynolds number regimes (and in many different works) is unlikely to be a mere coincidence. A possible explanation could be that these modes represent exact solutions in the state space of parallel shear flows (Pringle & Kerswell 2007; Duguet, Willis & Kerswell 2008). Although further studies are required in this direction, the consistency between VLSMs and the travelling wave instability with $\kappa_\theta \approx 3$ is important and further corroborated by the present results at high Reynolds numbers.
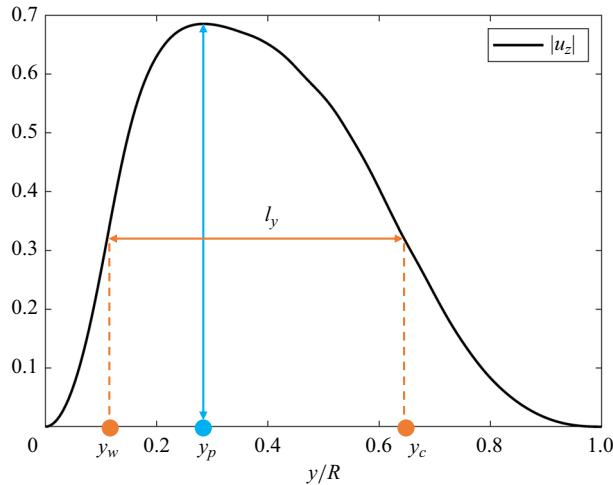
Figure 3. Illustration of the spatial characteristics of a generic POD mode. The modulus of the (complex) streamwise velocity is shown together with the height of the largest peak h (blue), the wall-normal position of the peak y_p and the thickness of the mode l_y (orange). The wall distances at half-amplitude, y_w and y_c, indicate the beginning and the end of the structure, respectively. The wall and the pipe centre are located at $y = 0$ and $y = R$, respectively. All the lengths are normalised by R.

4.3. *Spatial classification*

The POD analysis has proven valuable by providing insights into energy variations across the inhomogeneous wall-normal direction (Hellström *et al.* 2016). In the current formulation, the KL decomposition exploits the two homogeneous directions, defining one-dimensional modes (varying in the radial direction) for a given triplet $\boldsymbol{k} = (q, \kappa_\theta, \kappa_z) = (q, p)$. For each mode, we only consider the dominant peak, specifically using $q = 1$ for each triplet, which represents the most energetic structure within a wavenumber pair p. It is important to note that the below classification holds when all pairs are included, i.e. $q = 1, \ldots, \tilde{N}$ for each triple $\boldsymbol{k} = (q, p)$ (Massaro *et al.* 2024).

A MATLAB code is used to extract the spatial characteristics of the POD modes, as shown in figure 3. Each structure is characterised by the peak height (h), peak location (y_p) and mode thickness (l_y), all normalised by R. The size l_y represents the radial extension $l_y = y_c - y_w$. The coordinates y_w and y_c are the radial locations where the peak halves towards the wall ($y = R - r = 0$) and towards the centre ($y = 1$), respectively. The positions y_w and y_c mark the structure's start and end points, offering insight into the degree of asymmetry, as the peak is not necessarily symmetric. The depiction of the coordinates y_w and y_c as the positions where the peak halves occur is reasonable and customary, but to some extent arbitrary. Alternative definitions for assessing the size of the structure would yield a similar classification, albeit leading to a potentially unrealistic estimation of the radial thickness. The classification is conducted in spectral space for the streamwise velocity component u_z. The solid black line in figure 3 illustrates $|u_z|$ and the spatial characteristics of the POD mode for a generic $\boldsymbol{k} = (q = 1, p)$. Similar results are obtained by classifying in physical space and then averaging in the streamwise and azimuthal directions.

4.3.1. *Voronoi tessellation*

The KL decomposition produces spatially orthogonal modes whose energetic contributions add up to the total fluctuating kinetic energy. Therefore, when examining

the energy distribution in the radial direction, the density of POD modes at a particular location is essential, as their contributions are cumulative. An example at $Re_\tau = 2000$ is displayed in figure 4. In panel (*a*) each point represents the energy contribution of a mode with size l_y and the peak at radial position y_p. The intensity of the colour (over the blue-to-red range) indicates the mode's contribution to the total fluctuating energy. In panel (*b*) the contour plot of scattered points reveals a region with high energy between $0.12 < y_p/R < 0.5$ for $l_y/R > 0.45$ (upper vertex of the triangular contour plot). However, this plot represents the average energetic intensity and does not consider the density of the POD modes. Neglecting this aspect can lead to misleading results. For instance, a cluster of points at a specific y location may contribute more to the total energy than a single point with high energy at the same location. This issue has been highlighted by Massaro *et al.* (2024). Thus, the density of points (ρ) should be considered. When we weigh the energy contribution, it significantly alters the shape of the contour plot, as shown in figure 4(*c*). The radial classification based on energy reveals the emergence of two branches, although they are not fully separated at this Re_τ. These branches are classified and analysed in detail in the rest of this paper. Note that the contour plot undergoes substantial changes due to the consideration of the POD mode density. To accurately estimate the density ρ for each point, a Voronoi diagram is utilised.

Given a discrete set of points $\{x_j, y_j\}$ for $j = 1, \ldots, N_{TOT}$, the Voronoi diagram decomposes the space around each point (x_j, y_j) into a region of influence Ω_j, which ensures that any arbitrary point within Ω_j is closer to point j than to any other point. The Voronoi region Ω_j, with an area A_j, is referred to as the Voronoi region, and the collection of all these Voronoi regions forms the Voronoi diagram. A MATLAB algorithm was implemented to account for the external boundaries, where an infinite area of interest was generated. Further details can be found in Massaro *et al.* (2024), and an example is given in the supplementary material available at https://doi.org/10.1017/jfm.2024.776. The code defines an area (A_j) for each point, and the inverse of this area provides the density (ρ_j), representing the two-dimensional concentration of points. The Voronoi diagram, originally employed in fluid mechanics to describe the spatial structure of dispersed phases (Monchaux, Bourgoin & Cartellier 2010; García-Villalba, Kidanemariam & Uhlmann 2012), is now utilised to represent the spatial energy distribution of the POD modes.

4.4. *Attached and detached eddies*

The Voronoi-based contour plot effectively quantifies the energy, more precisely, the logarithm of the energy contribution weighted by its density. As the Reynolds number increases, a clear trend emerges, and two different classes of POD modes emerge. We begin by providing a comprehensive description of the spatial properties of these modes and how the Reynolds number affects the size of the most energetic structures (figure 5). Henceforth, the energy contribution, i.e. the ratio of the eigenvalue obtained by the KL decomposition $\lambda_{q,p}$ to the total kinetic energy k, is weighted by the Voronoi density ρ to account for the density of points in a region of the $(l_y/R, y_p/R)$ space. A logarithmic scale is used for $(\lambda_{q,p}/k)\rho$. Note that the plots depicted in figure 5 do not capture energy information near the wall ($y = 0$). This occurs as our analysis focuses specifically on LSMs, considering only the first 32 azimuthal and streamwise wavenumbers. Additionally, the classification of space is based on the location of the largest peak ($y_p/R = 0$), which accurately represents the near-wall location only in an idealised scenario, as depicted in figure 3. However, the shapes of POD modes are more complex and asymmetric. These factors contribute to the lack of populated regions near the wall. It is important to keep
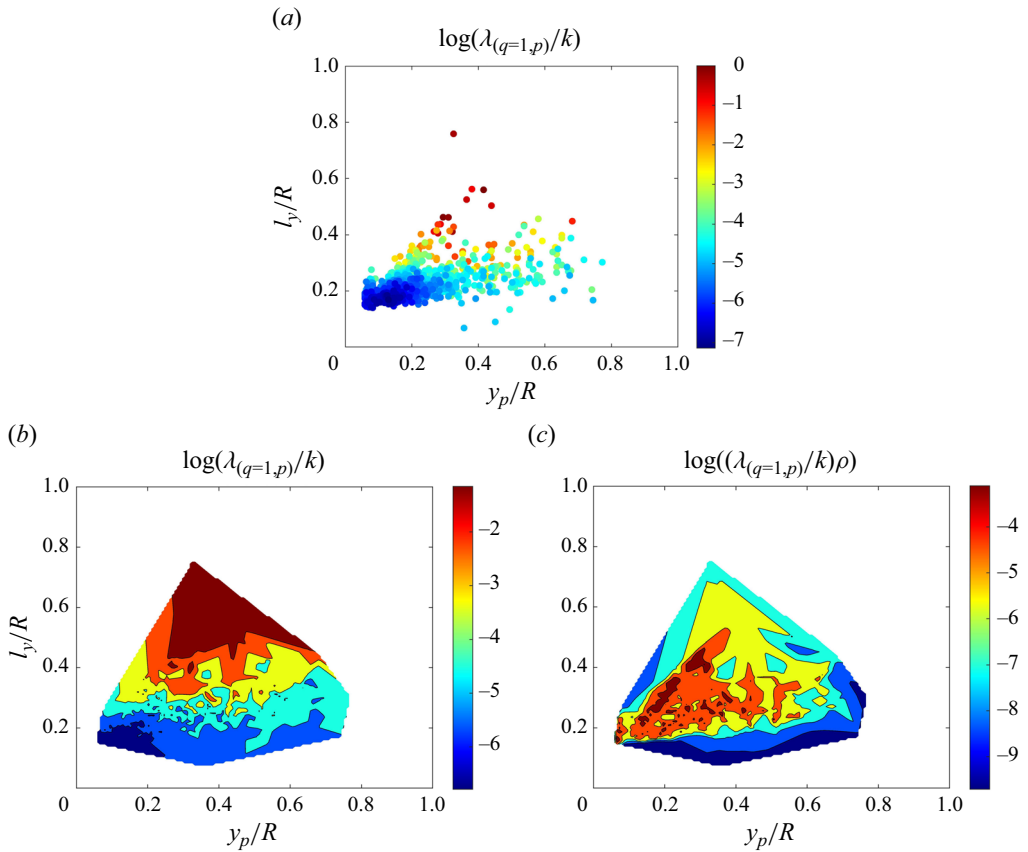
Figure 4. (*a*) Scatter plot of the points corresponding to the radial size of the POD mode (l_y) at the wall-normal location of the peak (y_p) at $Re_\tau = 2000$. The colour of the point indicates the energy content: the more intense the colour (in the blue–red scale), the more energetic the content is. (*b*) Contours of the energy in the scatter plot in (*a*). (*c*) Contours of the energy in the scatter plot in (*a*) weighted by the density estimated through the Voronoi tessellation.

these considerations in mind to avoid misinterpretation, as no near-wall filtering or shifting was applied.

In figure 5 a specific y_p/R point corresponds to the radial location of the largest peak of a structure that extends radially (not symmetrically) with a thickness denoted as l_y. At the lowest Reynolds numbers, the energy is concentrated in relatively small structures near the wall (Massaro *et al.* 2024). Omitting the discussion of the results at the intermediate $Re_\tau = 1000$ (which aligns with those at $Re_\tau = 2000$), we find that at $Re_\tau = 2000$, the energy is distributed across structures of varying sizes. The peak is located within a broad range of radial positions, specifically between $0.1R$ and $0.6R$. Among the most energetic structures, some exhibit peak positions beyond $0.5R$, near the centre of the pipe. In particular, the contour plot in (*a*) shows two distinct high-energy branches: the first is steep and extends up to $y/R \approx 0.4$ and the second reaches up to $y/R \approx 0.6$, but with a much lower slope. The distinction between these two classes of modes becomes even more obvious at $Re_\tau = 5200$, where the two branches are definitely set apart; see figure 5(*b*). The first family represents a highly energetic class of POD modes, with their size linearly correlated to the wall-normal distance of their peak, denoted as y_p. The inclined dashed line (class I) exhibits a slope of $l_y \sim 1.29y/R$ and $l_y \sim 1.20y/R$
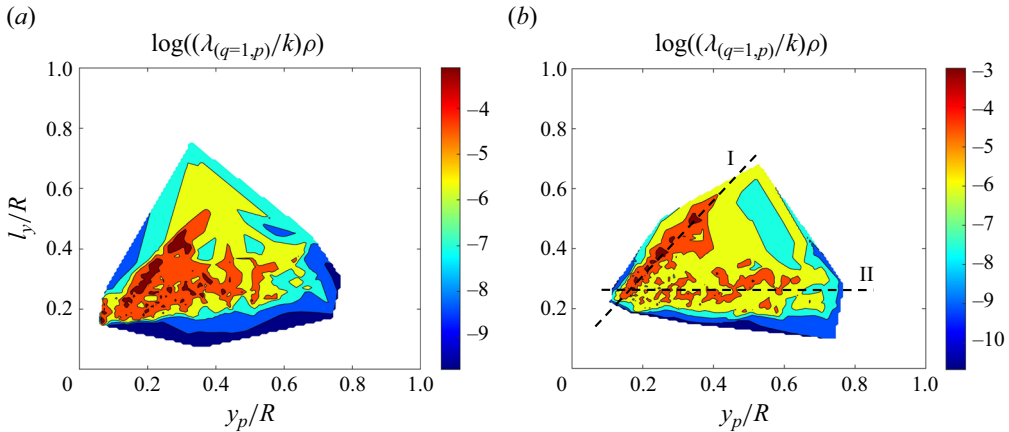
996 A45-14

Figure 5. Density-weighted energy contour of the scattered points $\{y_p, l_y\}$: y_p is the radial location of the largest peak and l_y is a measure of the structure's size. Plots (*a,b*) refer to $Re_\tau = 2000$ and 5200, respectively.

at $Re_\tau = 2000$ and 5200, respectively. The horizontal line represents another class of structures (class II) where the size remains nearly constant as the peak moves toward the centre of the pipe. The approximate values are $l_y \approx 0.25R$ at $Re_\tau = 2000$ and $l_y \approx 0.26R$ at $Re_\tau = 5200$, respectively.

However, the structure's size alone does not provide the complete picture. We also need to account for the degree of asymmetry. To this end, we calculate density-weighted contour plots for the starting (y_w) and ending (y_c) locations of the modes. Indeed, the energy distribution of the starting and ending points of the POD modes supports the classification into two distinct classes. At the two highest Reynolds numbers in the left panels of figure 6(*a,b*), two distinct branches are observed for y_w, which represents the wall-normal location of the beginning of the structures. The left panels show that the beginning of the detached eddies scales with y as these structures detach from the wall. The scaling relationship is $y_w \sim 0.836y/R$ at $Re_\tau = 2000$ and $y_w \sim 0.938y/R$ at $Re_\tau = 5200$. Additionally, the horizontal energetic branch near $y_w \approx 0$ represents modes where the beginning is 'attached' to the wall, meaning that y_w is constant over a range of y_p. As expected, the ending of the structures scales for both types of eddies, with linear trends of $y_c \sim 1.03y/R$ for both Reynolds numbers.

The sets of points in the two branches are extracted based on the high-energy content and linearly fitted in the least squares sense. The resulting classes are indeed distinct in terms of the axial and azimuthal wavenumbers. At both $Re_\tau = 2000$ and 5200, class I (attached) and class II (detached) include only POD modes with $\kappa_\theta > \kappa_z$ and $\kappa_\theta < \kappa_z$, respectively. According to the previous classification by Duggleby *et al.* (2007), these correspond to the wall and lift propagating modes, respectively, i.e. structures that turn azimuthally more than they lift axially ($\kappa_\theta > \kappa_z$) and that lift axially more than turning azimuthally ($\kappa_\theta < \kappa_z$). All the three highest Reynolds numbers depict these two classes, but, at $Re_\tau = 5200$, in particular, they are clearly distinct. Figure 7 shows the modes that belong to class I and class II with blue and black lines, respectively. As observed above, class I consists of eddies whose size scales linearly with the wall-normal distance, whereas the size remains constant for class II. Figure 7(*a*) is crucial, as it concisely illustrates the core distinction between wall-attached (blue lines) and detached (black lines) eddies. This illustration makes the definition of the term 'attached' evident, reflecting the model outlined in Perry & Chong (1982). At a low Reynolds number the classification
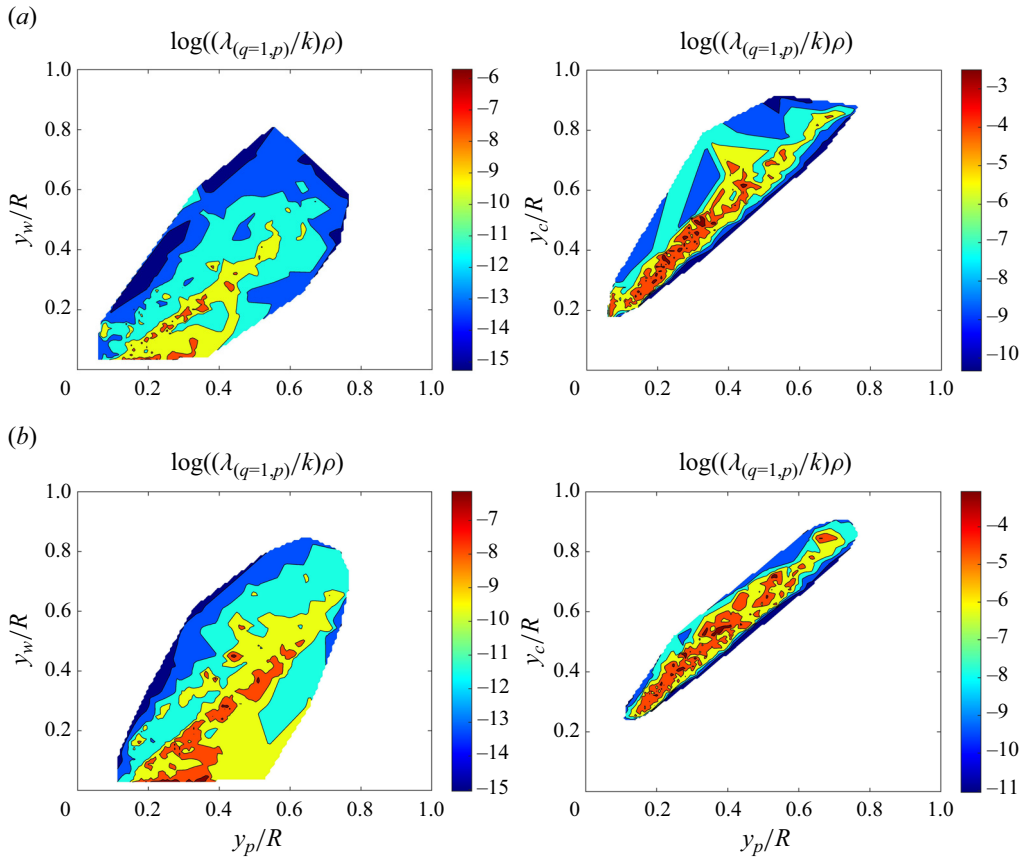
996 A45-15

(*a*)

(*b*)

Figure 6. Density-weighted energy contour of the scatter points (*left*) {y_p, y_w} and (*right*) {y_p, y_c}: y_p is the radial location of the highest peak, y_w and y_c are the wall-normal distances indicating the beginning and the end of the structure, respectively. Plots (*a*,*b*) refer to $Re_\tau = 2000$ and $Re_\tau = 5200$, respectively.

by Duggleby *et al.* (2007) indicates a comparable energy content between the wall and lift modes, i.e. classes I and II, respectively. At $Re_\tau = 5200$, the energy contained in the attached eddies is around 2 times larger than the energy in the detached eddies. This finding is of particular interest, especially in the context of the attached eddy model as discussed below.

As previously outlined, the size of the attached structures linearly scales with the wall-normal distance: $l_y \sim 1.29y/R$ and $l_y \sim 1.20y/R$ at $Re_\tau = 2000$ and $Re_\tau = 5200$, respectively. The result is consistent with the attached eddy model (Townsend 1976; Perry & Chong 1982) as well as the previous findings (Hu *et al.* 2020). As Re_τ increases, a trend is also observed, with the slope decreasing from 1.42 ($Re_\tau = 1000$) to 1.20 ($Re_\tau = 5200$). However, it is important to note that studying a simplified one-dimensional representation of the statistically coherent structures emerging from the KL decomposition has its limitations. For example, the behaviour of λ_z and $\lambda_{R\theta}$ as functions of y cannot be investigated, in contrast to other studies (Hwang 2015; Deshpande *et al.* 2021).

Eventually, the degree of asymmetry is also reported in figure 8 at $Re_\tau = 2000$ and 5200, respectively. The asymmetry of the mode is measured with respect to the radial location of the largest peak (y_p). The distance between where the structure begins (y_w) and the largest peak (y_p), and the distance between where the structure ends (y_c) and the largest
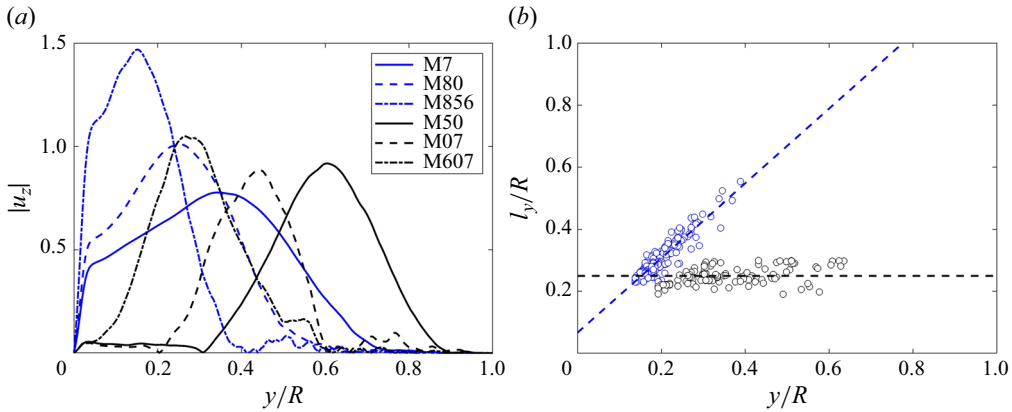
996 A45-16

Figure 7. (*a*) Modulus of the (complex) streamwise velocity of the POD modes belonging to the inclined (blue) and horizontal (black) branches. The legend indicates the POD mode number according to the global energy-based ordering. (*b*) The points belonging to the two red branches in figure 5 are extracted according to their energy level. As shown in (*a*), these correspond to attached and detached eddies, respectively. The dashed lines are obtained via linear regression in the least squares sense for the two sets of points, separately. Only data at $Re_\tau = 5200$ are considered in (*a,b*).
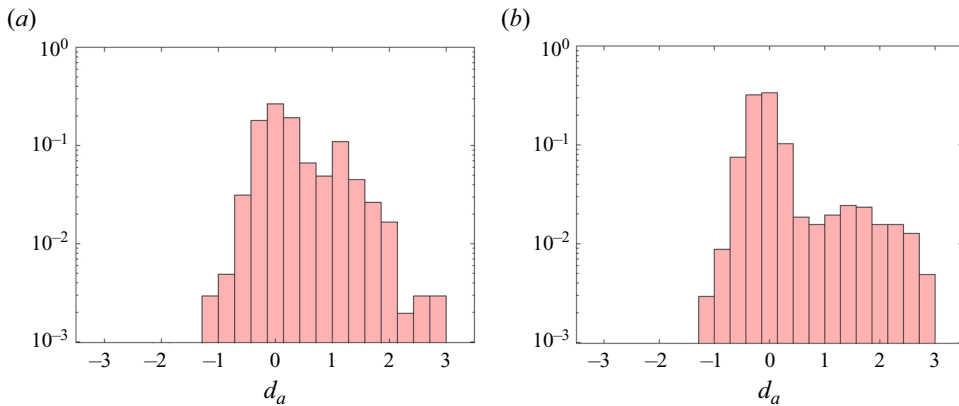
Figure 8. Histograms of the degree of asymmetry (d_a) are reported (with a constant unitary area for each diagram). Panels (*a,b*) refer to $Re_\tau = 2000$ and 5200, respectively.

peak (y_p) are used to estimate the asymmetry of the mode: $d_a = \log(|y_c - y_p|/|y_w - y_p|)$. For $d_a = 0$, the structure is perfectly symmetric. In both cases, most of the modes are symmetric. A few structures with a remarkably non-symmetric behaviour appear for $d_a > 2$ towards the centre of the pipe. These outliers are more numerous at higher Reynolds numbers. However, overall, the increase in the Reynolds number indicates a rise in the symmetry of the POD modes, with 64 % and 76 % of the modes falling within the range $|d_a| < 0.4$ at $Re_\tau = 2000$ and 5200, respectively.

4.5. *Modal self-similarity*

The POD modes in the azimuthal and streamwise directions are Fourier harmonics and, therefore, inherently self-similar. On the other hand, the modes in the radial direction are data driven, and their shape function is not known *a priori*. Following Hellström
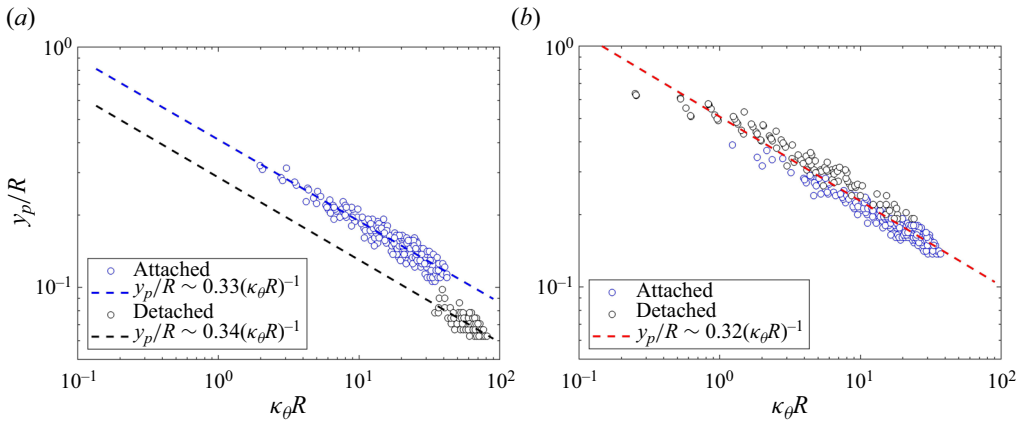
Figure 9. Modal self-similarity of the POD modes $\hat{\Phi}_{(q=1,p)}(r)$. Plots (*a*,*b*) refer to $Re_\tau = 2000$ and $Re_\tau = 5200$, respectively. The wall-normal length scale is estimated as radial extension y_p/R, with the scaling law $y_p/R \sim C(\kappa_\theta R)^{-1}$ and $C \approx 0.32$. Attached and detached eddies are shown in blue and black, respectively. The dashed lines are obtained via linear regression in the least squares sense for the two sets of points.

et al. (2016), we explore the self-similarity to examine the presence of a universal length scale for the attached and detached eddies. In this context, we specifically focus on the self-similarity of the modal peak location.

The azimuthal and radial length scales of the eddies are estimated as follows. For any POD mode $\hat{\Phi}_{(q=1,p)}(r)$, similar to the approach used in Hellström *et al.* (2016), we estimate the azimuthal wavelength as $\lambda_\theta = 2\pi(R - y_p)/\kappa_\theta$, where $(R - y_p)$ represents the radial location of the mode maximum. For the radial size, we employ the wall-normal location of the peak. In figure 9 we present the wall-normal (y_p/R) and the azimuthal length scale ($\kappa_\theta R$). In panel (*a*) the Reynolds number is reasonably close to the value in the experiments by Hellström *et al.* (2016), namely $Re_\tau = 2460$. The agreement is striking: the structure exhibits a self-similar behaviour over more than a decade of $\kappa_\theta R \in [2, 42]$, with a radial extension of $y_p/R \in [0.1, 0.3]$ (blue points). Similar to the findings in figure 5 of Hellström *et al.* (2016), our results also indicate a deviation for the smaller eddies. Hellström *et al.* (2016) suggest that this deviation is related to their proximity to the wall, implying that these eddies are influenced by the viscosity. They excluded these structures when estimating the scaling law. However, our previous energy-based classification allowed us to distinguish between the attached and detached eddies, represented in black and blue, respectively, in the various figures.

This distinction shows that the two clusters of points in figure 9(*a*) correspond to the two previously extracted classes of modes. Therefore, the black modes do not constitute a set of deviated POD modes but rather a topologically distinct set of modes, i.e. detached modes, which also exhibit self-similarity. In fact, by extrapolating the constant of linear scaling for these two groups individually, it becomes evident that they both exhibit self-similarity, with a similar constant $C \approx 0.3$. This value is in close agreement with the estimation by Hellström *et al.* (2016) at $Re_\tau = 2460$, where this 'deviating set of modes' was excluded since it was not previously identified as detached eddies. Nevertheless, as suggested by Hellström *et al.* (2016), this deviation is likely an effect of the low Reynolds number. Therefore, considering that the two classes are not very distinct at $Re_\tau = 2000$, as seen in figure 5(*a*), we also examine the highest Reynolds number, $Re_\tau = 5200$, where the two branches exhibit two distinct slopes; see figure 5(*b*). The set of points converges to a

996 A45-18

single, overlapping group of modes, showing a slope of $y_p/R \sim 0.32(\kappa_\theta R)^{-1}$. Figure 9(*b*) indicates a linear scaling for $\kappa_\theta R \in [0.2, 37]$. The most energetic structures located in the logarithmic and outer layers, which were categorised above as attached and detached eddies, clearly exhibit a single azimuthal length scale. The geometric self-similarity of the energy-containing motions, for both attached and detached eddies, is reported here for the first time as it necessitates a high Reynolds number and the subsequent separation of scales. This observation aligns with the findings of Hwang (2015) for turbulent channel flows and constitutes a fundamental aspect for models based on Townsend's AEH.

4.6. *Helix angle of the modes*

To comprehensively characterise the spatial arrangements of the attached and detached eddies within the logarithmic layer and above, we measure the dominant helix angle, which represents the azimuthal inclinations relative to the streamwise direction. For this analysis, we exclusively focus on the highest Reynolds number, namely $Re_\tau = 5200$, since an adequate separation of scales is needed. When examining instantaneous velocity streaks longer than $3R$ (as shown on the cylindrical shells in figure 1), they frequently exhibit relatively straight configurations, indicating minimal variation in their azimuthal inclinations with respect to the streamwise direction. While they may maintain constant angles on the shell (Baltzer *et al.* 2013), these extended streaks can take on the appearance of a helix in the three-dimensional space. Therefore, we now refer to the angle between the streamwise direction within a cross-stream plane (r, θ) as the 'helix angle'. The helix angle, denoted as α_h, can be either positive or negative, depending on whether the helix rotates clockwise or anticlockwise when viewed from a downstream location.

For the POD modes, the helix angle can be measured following the definition by Baltzer *et al.* (2013), where α_h is defined as

$$\alpha_h \approx \arctan\left(\frac{(R - y)2\pi\kappa_z}{L_z\kappa_\theta}\right), \tag{4.1}$$

a function of the wall-normal distance y, the axial length (L_z) and wavenumber (κ_z). In the current classification, we estimate α_h for each POD mode using the location of the largest peak (y_p). In 95.2 % of cases, both classes exhibit a helix angle below $6.5°$. This consistency with the helix angles measured in the instantaneous fluctuating axial-velocity structures and the dominant streaks of the two-point correlations by Baltzer *et al.* (2013) is noteworthy. Their study was conducted in a pipe of similar length ($30R$) and moderately high Reynolds number ($Re_\tau = 685$). They also performed POD and measured angles of $\approx 5.1°$ and $\approx 6.8°$ for the most energetic modes. The energy-based classification introduced above allows us to observe how the helix angles vary for the specific classes that contribute significantly to the energy, i.e. attached and detached eddies.

The two classes exhibit distinct helical behaviours. The attached eddies, primarily located in the logarithmic region ($y/R < 0.3$), consistently exhibit helix angles of less than $3.2°$; see figure 10(*a*). This results from the combination of two effects. First, the size of the attached eddies scales linearly with the wall-normal distance, as discussed earlier, but the peak does not shift significantly toward the centre of the pipe. Additionally, these modes can have large wavelengths; see figure 10(*c*). When these observations are combined in (4.1), the resulting helical twist remains relatively small (figure 10). In contrast, the detached eddies exhibit significant variability. As mentioned in the previous section, a clear separation between the two classes only occurs at the highest Reynolds number. This could potentially explain why Baltzer *et al.* (2013) did not report larger α_h values among the most energetic modes. The detached eddies maintain an almost constant size
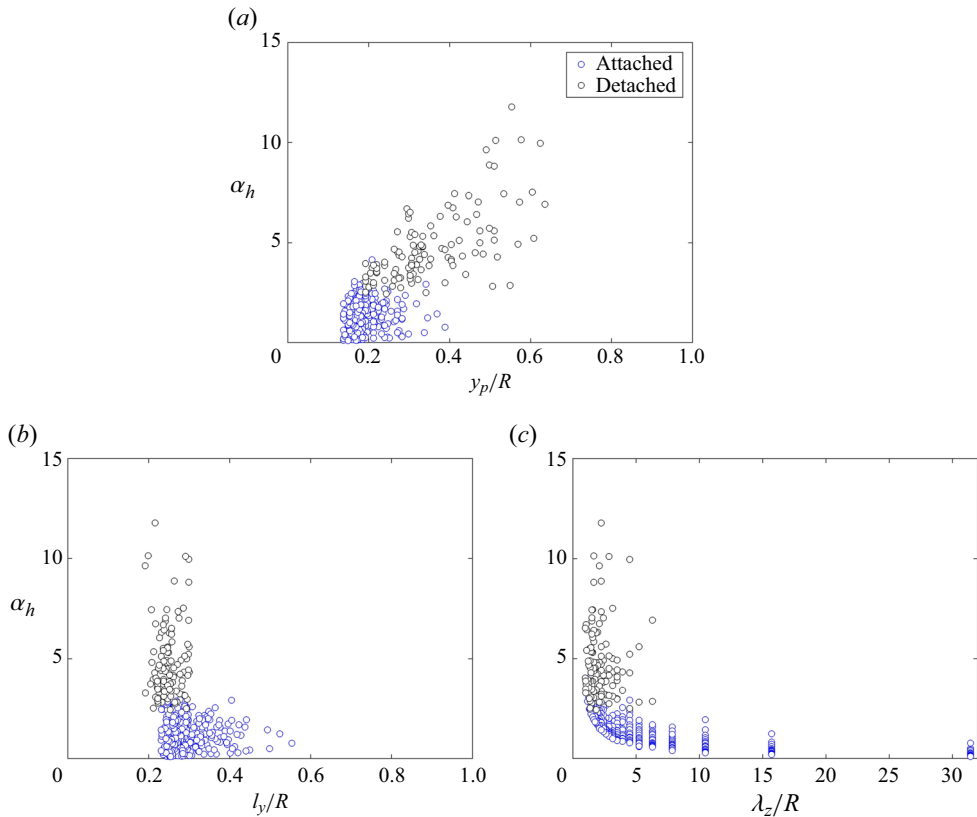
Figure 10. Helix angle of the attached (blue) and detached (black) POD modes $\hat{\Phi}_{(q=1,p)}(r)$, as a function of (*a*) the peak location, (*b*) the radial size of the mode and (*c*) the axial extension, i.e. the axial wavenumber. All the panels refer to $Re_\tau = 5200$.

regardless of their wall-normal location and have helix angles ranging between $3°$ and $7°$, with some outliers having a helix angle exceeding $7.5°$. The outlier modes do not have an exceptionally long streamwise length, with their axial wavelength always remaining below 5; see figure 10(*c*). However, they do exhibit a significant shift towards the centre of the pipe with a peak occurring around $y/R \approx 0.5$. This implies that as the eddies detach from the wall while maintaining an almost constant size, they progressively exhibit a larger twisting with an angle of up to $11.2°$. This is also evident in figure 11, where we present the POD modes 27 and 7, as examples. The attached eddy in figure 11(*a*) exhibits a smaller twist, with the streamwise velocity streaks remaining attached to the wall. In contrast, the detached mode in figure 11(*b*) displays a more pronounced twisting, attributed to a stronger azimuthal velocity.

Thus, the two classes exhibit distinctive helical characteristics. Remarkably, they share similarities with very long fluctuating axial motions and the two-point correlation, as reported in Baltzer *et al.* (2013). However, the POD modes display organised, periodic patterns around the circumference of the pipe. These vector patterns remain consistent for each POD mode as z varies, with the only variation being a rotation around the pipe axis in a helical manner. Note that while the counterclockwise modes are presented in figure 11, there is always an equivalent set of clockwise modes for oppositely signed wavenumbers. The only difference is that the azimuthal variations are mirror images of the
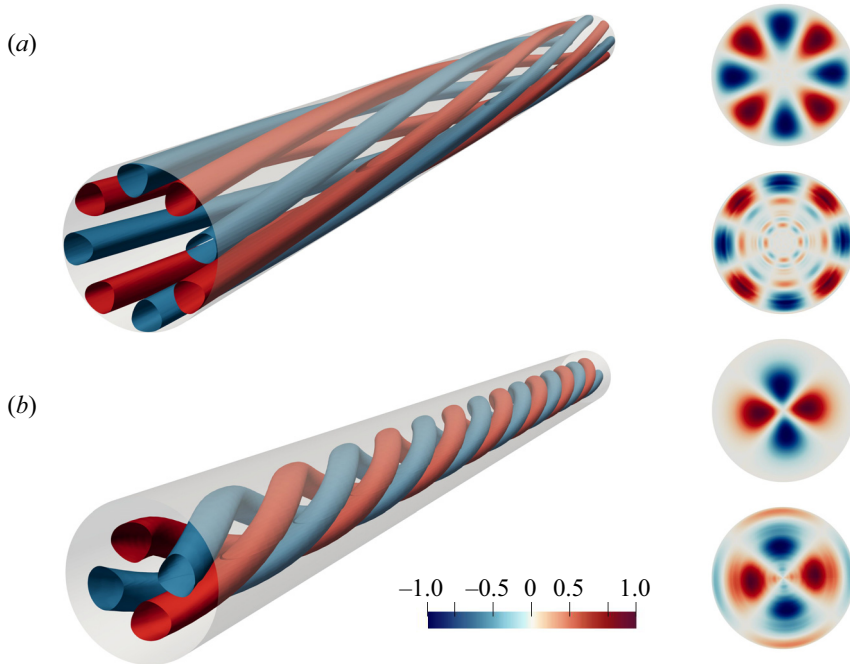
996 A45-20

Figure 11. Illustration of the spatial development and corresponding helical angle for the (*a*) attached and (*b*) detached POD mode with wavenumbers ($\kappa_\theta = 4$, $\kappa_z = 2$) and ($\kappa_\theta = 2$, $\kappa_z = 7$), respectively. From left to right: positive and negative three-dimensional isosurfaces of the axial velocity u_z (corresponding to 50 % of the maximum magnitude) and cross-stream planes of the radial and azimuthal velocity. Both panels refer to $Re_\tau = 5200$.

illustrated modes. In general, these motions exhibit characteristics resembling roll cells in a statistical sense. As a result, these mode patterns may not appear visually symmetric in the instantaneous planes, especially as they approach the core.

4.7. *Large- and very-large-scale motions*

Large-scale motions are commonly described as the coalescence of vortex packets generated when multiple structures travel at the same convective velocity (Kim & Adrian 1999; Adrian *et al.* 2000; Balakumar & Adrian 2007). In particular, LSMs involve the alignment of vortical structures within the packet in the streamwise direction, leading to the creation of zones with reduced streamwise momentum (Adrian *et al.* 2000; Ganapathisubramani, Longmire & Marusic 2003). In turbulent pipe flows, LSMs are associated with structures of a size of approximately $3R$ (Baltzer *et al.* 2013). In addition to these, energetic modes that are not only longer but also taller have been observed. These 'VLSMs' are defined as motions that are longer than the mean bulge length (Jiménez 1998; Kim & Adrian 1999). In the outer region of fully developed turbulent pipe flow, VLSMs reach wavelengths well beyond dozens of the pipe radius in length (Guala, Hommema & Adrian 2006; Monty *et al.* 2007). In this context, our objective is to identify whether the two previously detected classes correspond (or are related) to LSMs and VLSMs. Note that both sets of the POD modes, calculated for $\{N_\theta \times N_z\} = \{32, 32\}$, predominantly exhibit their largest peak in the outer layer. Figure 12 illustrates the regions of interest in the current study, which focuses on LSMs. Let us emphasise once more that the
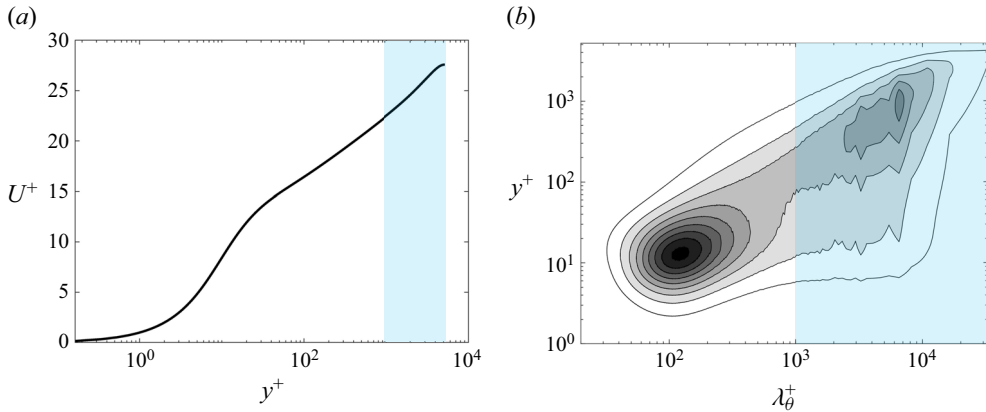
Figure 12. (*a*) Mean velocity profile and (*b*) wavenumber pre-multiplied energy spectrum $k_\theta E_{zz}/u_\tau^2$ for $Re_\tau = 5200$. The light-blue area refers to the locations where the largest peak of the most energetic modes for $\{N_\theta \times N_z\} = \{32, 32\}$ are located.

transparent light-blue region in figure 12 is not intended as a threshold for filtering, but rather represents an outcome of the energy-based classification.

The distribution of POD modes for each of the two classes is measured in terms of the axial size (l_z), the largest peak location (y_p) and the beginning/end of the structure. Probability density functions (PDFs) are obtained via histograms (with a constant unitary area for each diagram) and the conclusions drawn in this section are not affected by the binning choice. In figure 13(*a*) the PDF of the streamwise length is shown ($l_z = 10\pi R/\kappa_z$). Note that a distinction is necessary between the streamwise wavelengths defined using the streamwise Fourier decomposition and the streamwise wavelengths defined based on the presence of azimuthal wavering (Baltzer *et al.* 2013). In an experimental hot-wire rake measurement of turbulent pipe flow, Monty *et al.* (2007) observed exceptionally long streamwise velocity structures, reaching lengths of up to 25*R*. These structures exhibited a 180° rotation about the pipe axis, as well as meandering with large helix angles. This interpretation of sinusoidal meandering is in agreement with the view of attached eddies with high (and almost constant in *y*) helix angles. It is also consistent with the interpretation based on shorter streaks with azimuthal inclinations interacting with a helix angle varying in *z*. Both scenarios can generate two-point correlation patterns consistent with those observed in experiments (Monty *et al.* 2007; Baltzer *et al.* 2013). However, the current energy-based statistical approach makes it impossible to distinguish the two interpretations. An alternative decomposition based on dynamic evolution, such as dynamic mode decomposition (Schmid 2022), might provide additional insights. In that case, identifying the most 'relevant' mode becomes critical, as no clear hierarchy is inherently present.

In this section, our focus is not to delve into the mechanism of VLSM formation. Instead, we aim to quantify the presence of VLSMs and LSMs within the two energetic classes of attached and detached structures. Our findings strongly suggest that the VLSM structures are most likely attached. This conclusion is supported by the observation that all POD modes in class I (see figure 5) exhibit an elongation greater than 3*R* in the axial direction ($\kappa_z < 10$). In contrast, the detached eddies exhibit similarities to LSMs, with approximately 83 % of them having an axial extension smaller than 3*R* ($l_z \lesssim 3$). The few VLSMs within the detached eddies still have relatively short lengths, ranging from 3.1*R* to
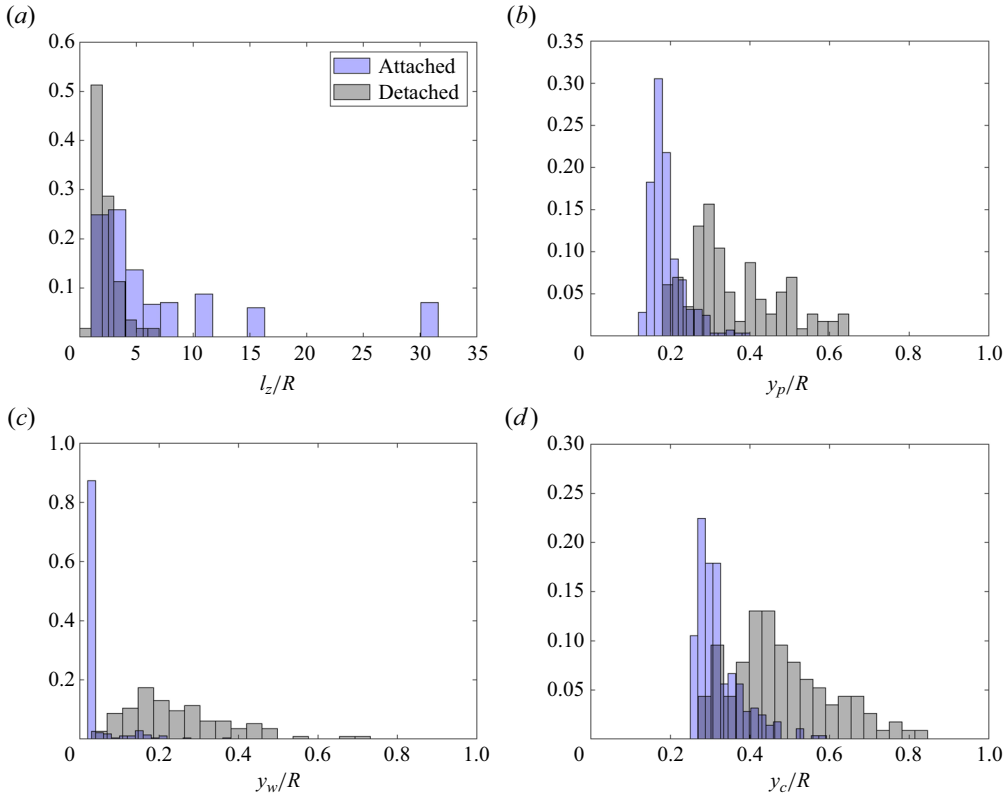
996 A45-22

Figure 13. Discrete PDF of the attached and detached eddies for (*a*) axial extension, (*b*) the largest peak location, (*c*) the beginning and (*d*) the ending of the POD mode in the radial direction. The blue and black areas are normalised to guarantee a unitary area. All the panels refer to $Re_\tau = 5200$.

$6.1R$, whereas the VLSM attached motions consistently exhibit lengths exceeding $8R$; see figure 13(*a*).

The largest peak location in the radial direction also exhibits an interesting pattern. In the case of attached eddies, i.e. VLSM, approximately 97.8 % of these structures have their peaks in the log region ($y/R < 0.3$), as shown in figure 13(*b*). Thus, the proposed characterisation outlines the attached nature of these motions; see figure 13(*c*). The beginning of these structures, denoted by y_w, is consistently located near the wall. These VLSMs typically terminate around $0.5R$, not extending far into the pipe's central region (figure 13*d*), consistently with the modes shown in figure 11. However, this situation changes for the detached motions. Only 33.1 % of them have the largest peak in the log layer, with structures progressively shifting towards the pipe centre. They reach up to a wall-normal distance of approximately $0.8R$, with their beginnings completely detached from the wall. Figure 13(*c*) clearly illustrates this detachment as structures become progressively more centralised.

5. Concluding remarks

We study the large-scale coherent structures in turbulent pipe flows at various Reynolds numbers ($Re_\tau = 180, 550, 1000, 2000$ and 5200) using data from DNS of Yao *et al.* (2023). We modally decompose the data through the KL bi-orthogonal expansion, also

commonly referred to as POD. The resulting POD modes are one-dimensional functions of the wall-normal distance and are arranged based on their energy content. A novel Voronoi-based analysis is employed to assess the cumulative energy contribution of the POD modes (Massaro *et al.* 2024). The study provides insights into the hierarchy of modes, their spatial characteristics and their dependency on the Reynolds number. We extract and explore structures from the outer region exclusively, i.e. a reduced set of the axial and azimuthal wavenumbers is considered.

As Re_τ increases, the contribution to the total turbulent energy (k) becomes more uniformly distributed among the modes. The POD modes with a streamwise wavenumber $\kappa_z = 0$, i.e. with an axial wavelength greater than $10\pi R$, emerge as the most energetic. This suggests a long spatial correlation, in a statistical sense. Similar structures have been documented in TBL flows by Hutchins & Marusic (2007), as well as in channels and lower-Reynolds-number pipe flows (Monty *et al.* 2007). At $Re_\tau = 1000, 2000$ and 5200, modes with an azimuthal wavenumber ($\kappa_\theta = 3$, $\kappa_z = 0$) are consistently observed among the most energetic. Similar modes were identified in transitional and turbulent pipe flows. Faisst & Eckhardt (2003) and Eckhardt *et al.* (2007) predicted nonlinear travelling wave instabilities with $\kappa_\theta = 3$ and Hof *et al.* (2004) identified similar states. The formation mechanism of these travelling waves in transitional flows is inherently unstable, making it challenging for these modes to persist in turbulent flow. However, the presence of roll modes with $\kappa_\theta = 3$ in various Reynolds number ranges (and in various works, as Guala *et al.* 2006; Bailey & Smits 2010; Baltzer *et al.* 2013; Hellström *et al.* 2016) is unlikely to be a coincidence. We suggest that these modes might represent the exact solutions in the state space of parallel shear flows (Pringle & Kerswell 2007; Duguet *et al.* 2008). Further research is needed in this direction, but the consistency between VLSMs and the travelling wave instability with $\kappa_\theta \approx 3$ is a remarkable finding.

The POD modes are characterised by assessing the radial energy distribution for a specific quantity of interest, such as the structure's size. We employ a Voronoi diagram to compute a density-weighted energy contour plot, which accounts for the density of structures in a particular region when determining the energy contribution, as detailed in Massaro *et al.* (2024). At high Reynolds numbers, this innovative representation effectively distinguishes two highly energetic classes of structures: class I, characterised by a thickness (l_y) that linearly scales with the wall-normal distance, and class II, with a size that remains (almost) constant. These two classes represent wall-attached and detached eddies. They are both modally self-similar and have helix angles typically below approximately $6.5°$. However, differences arise in their radial and axial distributions. Specifically, the attached eddies consist entirely of VLSMs, meaning that they are longer than $3R$, whereas the detached eddies are most likely LSMs. The attached eddies always have their largest peak located within the distance of $0.1R$ from the wall and extend into the central part of the pipe, reaching a wall-normal distance of approximately $0.5R$. Their size scales linearly with y, having slopes of $l_y \sim 1.29y/R$ and $l_y \sim 1.20y/R$ at $Re_\tau = 2000$ and 5200, respectively. In contrast, the detached eddies have an approximately constant size of $l_y \approx 0.25R$ at $Re_\tau = 2000$ and $l_y \approx 0.26R$ at $Re_\tau = 5200$, progressively moving away from the wall towards the central part of the pipe. Of particular interest is the behaviour in the central region of the pipe, as it may provide insights into the differences between the streamwise velocity in pipes and channels (Monty *et al.* 2009). Our study indicates that these differences are likely to be associated with detached eddies rather than attached ones. An interesting avenue for further research would be to compare the current results with the POD analysis of turbulent channel flow at a similarly high Reynolds number to gain a deeper understanding of these two classes of modes in distinct geometries. Speculating

about possible implications of the dominant role played by the very large scales in wall turbulence, POD also offers the opportunity to create a reduced-order model. Such a model can be useful for large eddy simulations or in generating turbulent inflow conditions. This is particularly valuable because the very-large-scale components are challenging to be statistically modelled.

To conclude, this study uses a novel classification that distinguishes between attached and detached eddies based solely on their energy contributions, thus eliminating the need for any threshold or filtering. The primary limitation of this approach remains the requirement of a sufficiently high Reynolds number to ensure a clear separation of scales. Nevertheless, the insights gained from examining attached and detached structures at high Reynolds numbers are significant and provide valuable contributions to advancing the numerical modelling of turbulent pipe flows and understanding the nature of the large- (and very-large-) scale motions in pipes, as well as other types of wall turbulence.

Author ORCIDs.

D. Massaro https://orcid.org/0000-0002-6712-8944;

J. Yao https://orcid.org/0000-0001-6069-6570;

S. Rezaeiravesh https://orcid.org/0000-0002-9610-9910;

F. Hussain https://orcid.org/0000-0002-2209-9270;

P. Schlatter https://orcid.org/0000-0001-9627-5903.

REFERENCES

ADRIAN, R., MEINHART, C. & TOMKINS, C. 2000 Vortex organization in the outer region of the turbulent boundary layer. *J. Fluid Mech.* **422**, 1–54.

ATZORI, M., VINUESA, R., LOZANO-DURÀN, A. & SCHLATTER, P. 2018 Characterization of turbulent coherent structures in square duct flow. *J. Phys.: Conf. Ser.* **1001** (1), 012008.

BAARS, W.J. & MARUSIC, I. 2020*a* Data-driven decomposition of the streamwise turbulence kinetic energy in boundary layers. Part 1. Energy spectra. *J. Fluid Mech.* **882**, A25.

BAARS, W.J. & MARUSIC, I. 2020*b* Data-driven decomposition of the streamwise turbulence kinetic energy in boundary layers. Part 2. Integrated energy and a1. *J. Fluid Mech.* **882**, A26.

BAILEY, S. & SMITS, A. 2010 Experimental investigation of the structure of large- and very-large-scale motions in turbulent pipe flow. *J. Fluid Mech.* **651**, 339–356.

BALAKUMAR, B.J. & ADRIAN, R.J. 2007 Large- and very-large-scale motions in channel and boundary-layer flows. *Phil. Trans. R. Soc.* A **365**, 665–681.

BALTZER, J., ADRIAN, R. & WU, X. 2013 Structural organization of large and very large scales in turbulent pipe flow simulation. *J. Fluid Mech.* **720**, 236–279.

BROWN, G.L. & ROSHKO, A. 1974 On the density effects and large structure in turbulent mixing. *J. Fluid Mech.* **64**, 775–816.

CHENG, C., WEIPENG, L., LOZANO-DURÀN, A. & HONG, L. 2019 Identity of attached eddies in turbulent channel flows with bidimensional empirical mode decomposition. *J. Fluid Mech.* **870**, 1037–1071.

DEL ÁLAMO, J.C. & JIMÉNEZ, J. 2003 Spectra of the very large anisotropic scales in turbulent channels. *Phys. Fluids* **15**, 41–44.

DEL ÁLAMO, J.C., JIMÉNEZ, J., ZANDONADE, P. & MOSER, R.D. 2006 Self-similar vortex clusters in the turbulent logarithmic region. *J. Fluid Mech.* **561**, 329–358.

DENG, S., PAN, C., WANG, J. & HE, G. 2018 On the spatial organization of hairpin packets in a turbulent boundary layer at low-to-moderate Reynolds number. *J. Fluid Mech.* **844**, 635–668.

DESHPANDE, R., DE SILVA, C.M., LEE, M., MONTY, J.P. & MARUSIC, I. 2021 Data-driven enhancement of coherent structure-based models for predicting instantaneous wall turbulence. *Intl J. Heat Fluid Flow* **92**, 108879.

DUGGLEBY, A., BALL, K.S., PAUL, M.R. & FISCHER, P.F. 2007 Dynamical eigenfunction decomposition of turbulent pipe flow. *J. Turbul.* **8**, N43.

DUGGLEBY, A., BALL, K.S. & SCHWAENEN, M. 2009 Structure and dynamics of low reynolds number turbulent pipe flow. *Phil. Trans. R. Soc.* **367**, 473–488.

DUGUET, Y., WILLIS, A. & KERSWELL, R.R. 2008 Transition in pipe flow: the saddle structure on the boundary of turbulence. *J. Fluid Mech.* **613**, 255–274.

ECKHARDT, B., SCHNEIDER, T.M., HOF, B. & WESTRWEEL, J. 2007 Turbulence transition in pipe flow. *Annu. Rev. Fluid Mech.* **39**, 447–468.

EITEL-AMOR, G., ÖRLÜ, R., SCHLATTER, P. & FLORES, O. 2015 Hairpin vortices in turbulent boundary layers. *Phys. Fluids* **27** (2), 025108.

FAISST, H. & ECKHARDT, B. 2003 Travelling waves in pipe flow. *Phys. Rev. Lett.* **91**, 224502.

GANAPATHISUBRAMANI, B., LONGMIRE, E.K. & MARUSIC, I. 2003 Characteristics of vortex packets in turbulent boundary layers. *J. Fluid Mech.* **478**, 35–46.

GARCÍA-VILLALBA, M., KIDANEMARIAM, A.G. & UHLMANN, M. 2012 DNS of vertical plane channel flow with finite-size particles: Voronoi analysis, acceleration statistics and particle-conditioned averaging. *Intl J. Multiphase Flow* **46**, 54–74.

GROSSE, S. & WESTERWEEL, J. 2011 Investigation of large-scale coherent motion in turbulent pipe flow by means of time resolved stereo-PIV. In *The Ninth International Symposium on Particle Image Velocimetry (PIV'11), Kobe, Japan*.

GUALA, M., HOMMEMA, S.E. & ADRIAN, R.J. 2006 Large-scale and very-large-scale motions in turbulent pipe flow. *J. Fluid Mech.* **554**, 521–542.

HAMILTON, J., KIM, J. & WALEFFE, F. 1995 Regeneration mechanisms of near-wall turbulence structures. *J. Fluid Mech.* **287**, 317–348.

HELLSTRÖM, L.H.O., GANAPATHISUBRAMANI, B. & SMITS, A.J. 2015 The evolution of large-scale motions in turbulent pipe flow. *J. Fluid Mech.* **779**, 701–715.

HELLSTRÖM, L.H.O., MARUSIC, I. & SMITS, A.J. 2016 Self-similarity of the large-scale motions in turbulent pipe flow. *J. Fluid Mech.* **792**, R1.

HELLSTRÖM, L.H.O., SINHA, A. & SMITS, A.J. 2011 Visualizing the very-large-scale motions in turbulent pipe flow. *Phys. Fluids* **23**, 011703.

HOF, B., VAN DOORNE, C.W.H., WESTERWEEL, J., NIEUWSTADT, F.T.M., FAISST, H., ECKHARDT, B., WEDIN, H., KERSWELL, R.R. & WALEFFE, F. 2004 Experimental observation of nonlinear travelling waves in turbulent pipe flow. *Science* **305**, 1594–1598.

HU, R., YANG, X.I.A. & ZHENG, X. 2020 Wall-attached and wall-detached eddies in wall-bounded turbulent flows. *J. Fluid Mech.* **885**, A30.

HUSSAIN, F. 1986 Coherent structures and turbulence. *J. Fluid Mech.* **173**, 303–356.

HUTCHINS, N. & MARUSIC, I. 2007 Evidence of very long meandering features in the logarithmic region of turbulent boundary layers. *J. Fluid Mech.* **579**, 1–28.

HWANG, Y. 2015 Statistical structure of self-sustaining attached eddies in turbulent channel flow. *J. Fluid Mech.* **767**, 254–289.

JEONG, J., HUSSAIN, F., SCHOPPA, W. & KIM, J. 1997 Coherent structures near the wall in a turbulent channel flow. *J. Fluid Mech.* **332**, 185–214.

JIMÉNEZ, J. 1998 The largest scales of turbulent wall flows. In *Proceedings of the Summer Program, Center for Turbulence Research, Stanford University*, p. 137–154.

JIMÉNEZ, J. 2018 Coherent structures in wall-bounded turbulence. *J. Fluid Mech.* **842**, P1.

JIMÉNEZ, J. & PINELLI, A. 1999 The autonomous cycle of near-wall turbulence. *J. Fluid Mech.* **389**, 335–359.

KARHUNEN, K. 1947 Uber lineare methoden in der wahrscheinlichkeitsrechnung. *Annu. Acad. Sci. Fenn.* **37**, 3–79.

KIM, H.T., KLINE, S.J. & REYNOLDS, W.C. 1971 The production of turbulence near a smooth wall in a turbulent boundary layer. *J. Fluid Mech.* **50**, 133–160.

KIM, K.C. & ADRIAN, R.J. 1999 Very-large-scale motion in the outer layer. *Phys. Fluids* **11**, 417–422.

KOVASZNAY, L., KIBENS, V. & BLACKWELDER, R. 1970 Large-scale motion in the intermittent region of a turbulent boundary layer. *J. Fluid Mech.* **41**, 283–325.

LEE, M. & MOSER, R. 2019 Spectral analysis of the budget equation in turbulent channel flows at high Reynolds number. *J. Fluid Mech.* **860**, 886–938.

LOÈVE, M. 1948 *Fonctions Aleatoires du Second Ordre. Processus Stochastiques et Mouvement Brownien*, 1st edn. Gauthier-Villars.

LOZANO-DURÀN, A., FLORES, O. & JIMÉNEZ, J. 2012 The three-dimensional structure of momentum transfer in turbulent channels. *J. Fluid Mech.* **694**, 100–130.

LUMLEY, J.L. 1967 The structure of inhomogeneous turbulence. *Atmos. Turbul. Radio Wave Propag.* **6**, 166–177.

LUMLEY, J.L. 1970 *Stochastic Tools in Turbulence*. Elsevier.

MASSARO, D. 2024 Space-adaptive simulation of transition and turbulence in shear flows. PhD thesis, KTH Royal Institute of Technology.

MASSARO, D., YAO, J., REZAEIRAVESH, S., SCHLATTER, P. & HUSSAIN, F. 2024 Karhunen–Loève decomposition of high Reynolds number turbulent pipe flows: a Voronoi analysis. *J. Phys.: Conf. Ser.* **2753**, 012018.

MCKEON, B.J. & SHARMA, A.S. 2010 A critical-layer framework for turbulent pipe flow. *J. Fluid Mech.* **658**, 336–382.

MOISY, F. & JIMÉNEZ, J. 2004 Geometry and clustering of intense structures in isotropic turbulence. *J. Fluid Mech.* **513**, 111–133.

MONCHAUX, R., BOURGOIN, M. & CARTELLIER, A. 2010 Preferential concentration of heavy particles: a voronoi analysis. *Phys. Fluids* **22**, 103304.

MONTY, J.P., HUTCHINS, N., NG, H.C.H., MARUSIC, I. & CHONG, M.S. 2009 A comparison of turbulent pipe, channel and boundary layer flows. *J. Fluid Mech.* **632**, 431–442.

MONTY, J.P., STEWART, J.A., WILLIAMS, R.C. & CHONG, M.S. 2007 Large-scale features in turbulent pipe and channel flows. *J. Fluid Mech.* **589**, 147–156.

OLIVER, T.A., MALAYA, N., ULERICH, R. & MOSER, R.D. 2014 Estimating uncertainties in statistics computed from direct numerical simulation. *Phys. Fluids* **26**, 035101.

PERRY, A.E. & CHONG, M.S. 1982 On the mechanism of wall turbulence. *J. Fluid Mech.* **119**, 173–217.

PERRY, A.E. & MARUSIC, I. 1995 A wall-wake model for the turbulence structure of boundary layers. Part 1. Extension of the attached eddy hypothesis. *J. Fluid Mech.* **298**, 361–388.

PIROZZOLI, S., ROMERO, J., FATICA, M., VERZICCO, R. & ORLANDI, P. 2021 One-point statistics for turbulent pipe flow up to $Re_\tau \approx 6000$. *J. Fluid Mech.* **926**, A28.

PRINGLE, C.C.T. & KERSWELL, R.R. 2007 Asymmetric, helical, and mirror-symmetric traveling waves in pipe flow. *Phys. Rev. Lett.* **99**, 074502.

REZAEIRAVESH, S., XAVIER, D., VINUESA, R., YAO, J., HUSSAIN, F. & SCHLATTER, P. 2022 Estimating uncertainty of low- and high-order turbulence statistics in wall turbulence. In *Twelfth International Symposium on Turbulence and Shear Flow Phenomena*.

ROBINSON, S.K. 1991 Coherent motions in the turbulent boundary layer. *Annu. Rev. Fluid Mech.* **23**, 601–639.

SCHLATTER, P., LI, Q., ÖRLÜ, R., HUSSAIN, F. & HENNINGSON, D.S. 2014 On the near-wall vortical structures at moderate Reynolds numbers. *Eur. J. Mech.* B/*Fluids* **48**, 75–93.

SCHMID, P.J. 2022 Dynamic mode decomposition and its variants. *Annu. Rev. Fluid Mech.* **54** (1), 225–254.

SCHOPPA, W. & HUSSAIN, F. 2002 Coherent structure generation in near-wall turbulence. *J. Fluid Mech.* **435**, 57–108.

SHARMA, A.S. & MCKEON, B.J. 2013 On coherent structure in wall turbulence. *J. Fluid Mech.* **728**, 196–238.

SIROVICH, L. 1987*a* Turbulence and the dynamics of coherent structures. 2. Symmetries and transformations. *Q. Appl. Maths* **45**, 573–582.

SIROVICH, L. 1987*b* Turbulence and the dynamics of coherent structures. Part 1. Coherent structures. *Q. Appl. Maths* **45**, 561–571.

TOWNSEND, A.A. 1951 The structure of the turbulent boundary layer. *Math. Proc. Camb. Philos. Soc.* **47**, 375–395.

TOWNSEND, A.A. 1961 Equilibrium layers and wall turbulence. *J. Fluid Mech.* **11**, 97–120.

TOWNSEND, A.A. 1976 *The Structure of Turbulent Shear Flow*, 2nd edn. Cambridge University Press.

TROPEA, C., YARIN, A.L. & FOSS, J.F. 2007 *Springer Handbook of Experimental Fluid Mechanics*, 1st edn. Springer.

WALLACE, J.M., ECKELMAN, H. & BRODKEY, R.S. 1972 The wall region in turbulent shear flow. *J. Fluid Mech.* **54**, 39–48.

WANG, L., PAN, C. & WANG, J. 2022*a* Wall-attached and wall-detached eddies in proper orthogonal decomposition modes of a turbulent channel flow. *Phys. Fluids* **34**, 095124.

WANG, L., PAN, C., WANG, J. & GAO, Q. 2022*b* Statistical signatures of u component wall-attached eddies in proper orthogonal decomposition modes of a turbulent boundary layer. *J. Fluid Mech.* **944**, A26.

WEBBER, G.A., HANDLER, R.A. & SIROVICH, L. 1997 The Karhunen–Loève decomposition of minimal channel flow. *Phys. Fluids* **9** (4), 1054–1066.

WILLIS, A.P. 2017 The Openpipeflow Navier–Stokes solver. *SoftwareX* **6**, 124–127.

WILLMARTH, W.W. & LU, S.S. 1972 Structure of the reynolds stress near the wall. *J. Fluid Mech.* **55**, 65–92.

WU, X., BALTZER, J.R. & ADRIAN, R.J. 2012 Direct numerical simulation of a 30R long turbulent pipe flow at $R^+ = 685$: large- and very large-scale motions. *J. Fluid Mech.* **698**, 235–281.

YAO, J., REZAEIRAVESH, S., SCHLATTER, P. & HUSSAIN, F. 2023 Direct numerical simulations of turbulent pipe flow up to $Re_\tau \approx 5200$. *J. Fluid Mech.* **956**, A18.

ZAMAN, K.B.M.Q. & HUSSAIN, A.K.M.F. 1981 Taylor hypothesis and large-scale coherent structures. *J. Fluid Mech.* **112**, 379–396.